Comparison of Two-Temperature and Multifrequency Group Models of Radiative Transfer - Applied to Microfireball Dynamics in Light Ion Fusion Target Chambers

M. Uesaka and G.A. Moses

August 1983

UWFDM-534

FUSION TECHNOLOGY INSTITUTE

UNIVERSITY OF WISCONSIN

MADISON WISCONSIN

Comparison of Two-Temperature and Multifrequency Group Models of Radiative Transfer - Applied to Microfireball Dynamics in Light Ion Fusion Target Chambers

M. Uesaka and G.A. Moses

Fusion Technology Institute
University of Wisconsin
1500 Engineering Drive
Madison, WI 53706

http://fti.neep.wisc.edu

August 1983

UWFDM-534

COMPARISON OF TWO-TEMPERATURE AND MULTIFREQUENCY GROUP MODELS

OF RADIATIVE TRANSFER - APPLIED TO MICROFIREBALL DYNAMICS

IN LIGHT ION FUSION TARGET CHAMBERS

M. Uesaka

G.A. Moses

Fusion Engineering Program
Nuclear Engineering Department
University of Wisconsin-Madison
Madison, Wisconsin 53706

August 1983

I. Introduction

The reaction chamber in light ion beam driven fusion systems, both reactors and near term high gain target test facilities, will contain a gas at a pressure in the range of 1-50 torr. This gas is present to support the formation of z-pinch plasma channels to space charge and current neutralize the ion beams as they are propagated from the diodes to the target [1]. This gas also plays a significant role in the dynamics of the target microexplosion following ignition and thermonuclear burn. Soft target x-rays and ionic debris are stopped in a small volume of gas surrounding the target thus creating a microfireball. This fireball then propagates to the first wall, imparting both a radiative heat flux and shock overpressure to it (Fig. 1). The prediction of this heat flux and overpressure is vital to the thermal and mechanical design of the first wall.

For several years, this microfireball behavior has been examined using radiation hydrodynamics codes [2-8]. With the exception of the work by Sweeney [2] at Sandia Laboratory and some recent work by Uesaka [7] at the University of Wisconsin this analysis has been done using a two-temperature approximation for the plasma-radiation system. In this paper we report upon a comparison of the two-temperature and multifrequency group models of the plasma-radiation field for target yields and gas pressures that are expected to be relevant to both high gain target test facilities and eventually to ICF reactors. The results of this work include a set of guidelines for the accuracy of the two-temperature or the more computationally expensive multifrequency model for different gas types and pressures. We also include an explanation of the physical processes that are responsible for the differences
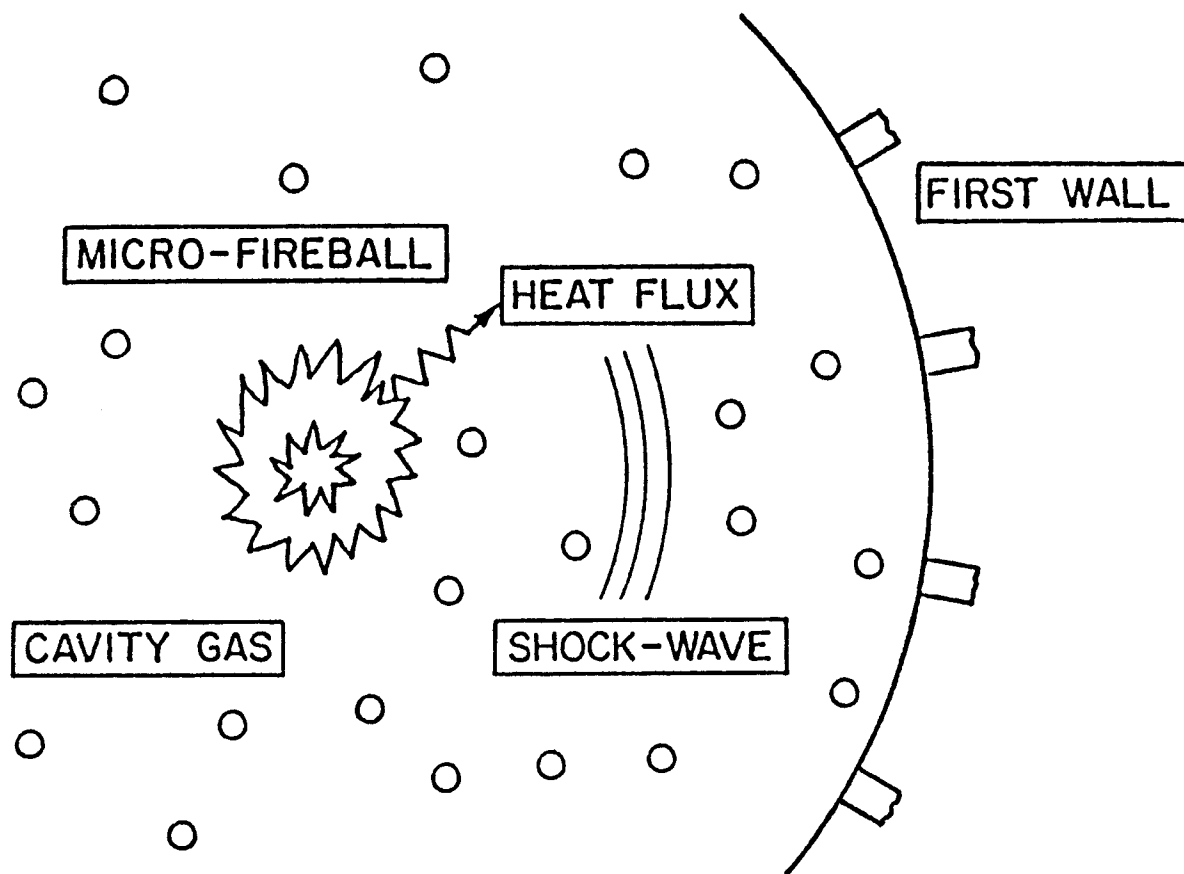
1

Fig. 1. Schematic picture of target explosion in a gas filled chamber.

of the two models, thus gaining more insight into the dynamics of ICF target generated microfireballs.

Section II of the paper describes the radiation-hydrodynamics model used in these calculations. Section III covers the results of the model comparison and contains an explanation for the differences in the results. Section IV is the summary and conclusions.

II. Description of the Radiation Hydrodynamics Computer Model

The MF-FIRE code has been developed to simulate the response of a gas to the x-rays and ionic debris emanating from an exploding inertial confinement fusion target [8]. The one-fluid hydrodynamic approximation is used and the one-dimensional equation of motion is expressed in Lagrangian coordinates as

$$\frac{\partial u}{\partial t} = - r^{\delta-1} \frac{\partial}{\partial m_0} (P + Q) + \dot{u}_d \tag{1}$$

where m_0 is the Lagrangian mass defined as

$$dm_0 = r^{\delta-1} \rho(r) \, dr \; .$$

The other quantities are the fluid velocity u, the total pressure P, the mass density ρ and one spatial dimension r ($\delta = 1$ planar, $\delta = 2$ cylindrical, $\delta = 3$ spherical). The term $\dot{u}_d$ is the velocity change in the fluid due to momentum deposition from debris. The plasma pressure, P_p, is computed from the perfect gas law,

$$P_p = n_p(1 + Z) \, k_B T_p \tag{2}$$

3

where Z is the charge state of the plasma, n_p is the number density of plasma atoms and T_p is the plasma temperature. The radiation pressure, P_R, is computed from the radiation energy density, E_R, by

$$P_R = \frac{1}{3} E_R \qquad (3)$$

where the radiation energy density has been assumed to be isotropic. The standard shock treatment using the Von Neumann artificial viscosity Q is used [9].

The plasma electrons and ions are assumed to be in equilibrium with each other so that the plasma can be characterized by a single local temperature $T_p(r,t)$. Thermal energy flow through the plasma includes electron thermal conduction and radiation diffusion. Radiation diffusion is treated by two methods, a two-temperature approximation and multifrequency approximation. In the two-temperature approximation, the radiation field is modeled as a fluid with its own local temperature $T_R(r,t)$, corresponding to a blackbody frequency spectrum. The two coupled diffusion equations are simultanteously and implicitly solved for the thermal transport in the plasma. These are

$$C_v \frac{\partial T_p}{\partial t} = \frac{\partial}{\partial m_o} (r^{\delta-1} K_p \frac{\partial T_p}{\partial r}) - \frac{\partial P_p}{\partial T_p} \dot{V} T_p - Q\dot{V} + \omega_R E_R - \omega_p T_p + S \qquad (4)$$

$$V \frac{\partial E_R}{\partial t} = \frac{\partial}{\partial m_o} (r^{\delta-1} K_R \frac{\partial E_R}{\partial r}) - \frac{4}{3} E_R \dot{V} \qquad - \omega_R E_R + \omega_p T_p \qquad (5)$$

where E_R is the radiation energy density, C_v is the specific heat at constant volume, Q is the artificial viscosity, V is the plasma specific volume, K_p and K_R are the plasma and radiation thermal conductivities, ω_R and ω_p are the

4

radiation absorption and emission coefficients and S is the rate that internal energy is added by the debris. The radiation temperature is obtained using the well-known expression,

$$E_R = \frac{4\sigma T_R^4}{c} \tag{6}$$

where σ is the Stefan-Boltzmann constant and c is the speed of light. The expression for the plasma thermal conductivity is the theoretical expression developed for electrons interacting with stationary ions [10] as

$$K_p = 20 \left(\frac{2}{\pi}\right)^{3/2} \frac{T^{5/2}}{\sqrt{m_e}\ e^4 (Z + 4) \ln \Lambda} \tag{7}$$

where e is the electron charge, m_e is the electron mass and $\ln \Lambda$ is the Coulomb logarithm. The radiation thermal conductivity and the radiation absorption and emission coefficients are related to the opacities by the expressions,

$$K_R = \frac{cV}{3\sigma_R(T_R,T_p)} \ ,$$

$$\omega_R = c\sigma_p(T_R,T_p) \ ,$$

$$\omega_p = 4\sigma T_p^3 \sigma_p(T_p)$$

where $\sigma_R(T_R,T_p)$ is the Rosseland opacity and $\sigma_p(T_R,T_p)$ and $\sigma_p(T_p)$ are the nonequilibrium and equilibrium Planck opacities. In the multifrequency approximation, we have rewritten Eqs. (4) and (5) as

$$C_v \frac{\partial T_P}{\partial t} = \frac{\partial}{\partial m_o} \left(r^{\delta-1} K_P \frac{\partial T_P}{\partial r} \right) - \frac{\partial P_P}{\partial T_P} \dot{V} T_P - Q\dot{V} + A - J + S \qquad (8)$$

$$V \frac{\partial E_R^g}{\partial t} = \frac{\partial}{\partial m_o} \left(r^{\delta-1} K_R^g \frac{\partial E_R^g}{\partial r} \right) - \frac{4}{3} E_R^g \dot{V} - c\sigma_P^g E_R^g + J^g , \qquad g = 1, \ldots, G \qquad (9)$$

where $\qquad E_R^g = \int_{h\nu_g}^{h\nu_{g+1}} dh\nu\, E_R(r,h\nu,t)$,

$$A^g = c\sigma_P^g E_R^g ,$$

$$J^g = \frac{8\pi K_B T_P^4}{c^2 h^3} \sigma_P^g \int_{x_g}^{x_{g+1}} dx\, \frac{x^3}{e^x - 1} , \qquad x = \frac{h\nu}{K_B T_P} ,$$

$$\qquad (10)$$

$$K_R^g = \frac{cV}{3\sigma_R^g} ,$$

$$A = \sum_{g=1}^{G} A^g ,$$

$$J = \sum_{g=1}^{G} J^g .$$

K_R^g is the radiation conductivity for frequency group g, J^g is the rate of radiation emitted by the plasma into group g and σ_P^g and σ_R^g are the Planck and Rosseland opacities for group g. In the MF-FIRE code, 20 energy groups are used as shown in Table 1. This set of G + 1 equations is not solved simultaneously as in the two-temperature model. Instead the multigroup equations are first solved individually and the terms A and J are computed. These terms are then explicitly included in the plasma temperature diffusion equation which is solved next.

An adjustment is added to the solution of these nonlinear diffusion equations to ensure physical relevance and numerical stability. The radiation

Table 1. Range of Radiation Energy Groups

Group Number	Energy Range (eV)
1	3×10^{-3} – 1
2	1 – 3
3	3 – 5
4	5 – 7.5
5	7.5 – 10
6	10 – 15.6
7	15.6 – 19
8	19 – 25
9	25 – 29.47
10	29.47 – 48.7
11	48.7 – 75
12	75 – 100
13	100 – 125
14	125 – 150
15	150 – 200
16	200 – 300
17	300 – 400
18	400 – 500
19	500 – 1000
20	1000 – 20000

diffusion equation is flux-limited. The flux across a zone boundary is not allowed to exceed cE_R, which is the free-streaming limit of radiation flux in a vacuum.

A most important feature of this model is the equation of state and radiative property data. For the MF-FIRE code, these data are stored in tabular form as a function of density, plasma temperature and radiation temperature. The tabulated quantities include: charge state $Z(n_p,T_p)$, plasma specific internal energy $e_p(n_p,T_p)$, Planck and Rosseland opacities $\sigma_p(n_p,T_p,T_R)$, $\sigma_R(n_p,T_p,T_R)$, multigroup Planck and Rosseland opacities $\sigma_p^g(n_p,T_p)$, $\sigma_R^g(n_p,T_p)$. These quantities are computed using a semi-classical model of the atom by the code, MIXERG [11].

The time required for the deposition of target x-rays into the cavity gas ($\sim 10^{-8}$ s) is much shorter than the hydrodynamic response time, so the gas is stationary as the x-rays are deposited. Hence, the thermodynamic state of the gas after x-ray deposition can be used as an initial condition in computing the gas response to the exploding target. The MF-FIRE code allows the target x-ray spectrum to be broken up into 20 groups (different from the radiation diffusion group structure) and assumes exponential attenuation of each group, which should be adequate for most target x-ray spectra. The initial x-rays that are photoabsorbed by the gas reduce the number of bound electrons available to interact with subsequent x-rays, so the attenuation coefficient decreases as x-rays are deposited. This is called the x-ray bleaching effect. A method of modifying the photoelectric attenuation coefficient of the gas to account for increasing ionization has been included in the MF-FIRE code to simulate this bleaching effect [12].

III. Fireball Calculation and Comparison of the Two-Temperature Model with the Multifrequency Model

1. Fireball Calculation

We have used the two-temperature model and the multifrequency model for radiation transport with the opacity data from MIXERG to simulate the behavior of fusion target generated microfireballs. We have compared the results of these two models to check the validity of the two-temperature model. For all calculations, a target yield of 200 MJ and a 3 meter radius first wall were used. Argon and nitrogen cavity gases were considered in this study. Both the noble argon gas and the molecular nitrogen gas are likely candidates for a background gas to support the formation of plasma channels. We chose several mass densities of 2.50×10^{-6} g/cm^3 through 4.17×10^{-5} g/cm^3, among which the mass density of 2.25×10^{-5} g/cm^3 was thought to be the best for channel formation according to our current understanding [1]. The input parameters are summarized in Table 2.

For these calculations we used a target design originally proposed by Bangerter [13] and shown in Fig. 2. Subsequently, Moses analyzed this target and characterized its x-ray, debris, and neutron output [14] using the PHD-IV code [15]. Bangerter's original design gave a nominal yield of 100 MJ and Moses's analysis followed this design. The 200 MJ of target output for this study is obtained by simply multiplying Moses' results by a factor of two. The x-ray spectrum emerging from the 200 MJ target is shown in Fig. 3. Here, 27% of the target yield is released as x-rays and debris. In our calculation the pellet x-ray energy is deposited in the gas at t = 0 s. Rather than using the dynamic target debris slowing down option in MF-FIRE the deposition of the debris energy is simulated by adding the debris energy to the lowest x-ray

9

Table 2. Gas Parameters for Comparison Calculations

Nitrogen			Argon		
Mass Density (g/cm^3)	Number Density (cm^{-3})	Pressure at 0°C (torr)	Mass Density (g/cm^3)	Number Density (cm^{-3})	Pressure at 0°C (torr)
4.17×10^{-5}	1.79×10^{18}	50	4.17×10^{-5}	6.22×10^{17}	18.5
2.25×10^{-5}	9.68×10^{17}	27	2.25×10^{-5}	3.39×10^{17}	10.0
1.33×10^{-5}	5.74×10^{17}	16	1.33×10^{-5}	1.99×10^{17}	5.93
8.33×10^{-6}	3.59×10^{17}	10	8.33×10^{-6}	1.24×10^{17}	3.70
4.12×10^{-6}	1.79×10^{17}	5	4.12×10^{-6}	6.22×10^{16}	1.85
2.50×10^{-6}	1.08×10^{17}	3			

Cavity Radius   = 3 meters

Target Yield   = 200 MJ

Initial Gas Temperature = 0.1 eV

ION BEAM FUSION TARGET WITH
LOW DENSITY PUSHER

Pb

TAMPER $\rho = 11.3$ (72.1 mg)

PUSHER $\rho = 1.26$
(16.8 mg)

FUEL $\rho = 0.21$
(1.00 mg)

Ta COH

DT

VOID

0.23333 cm
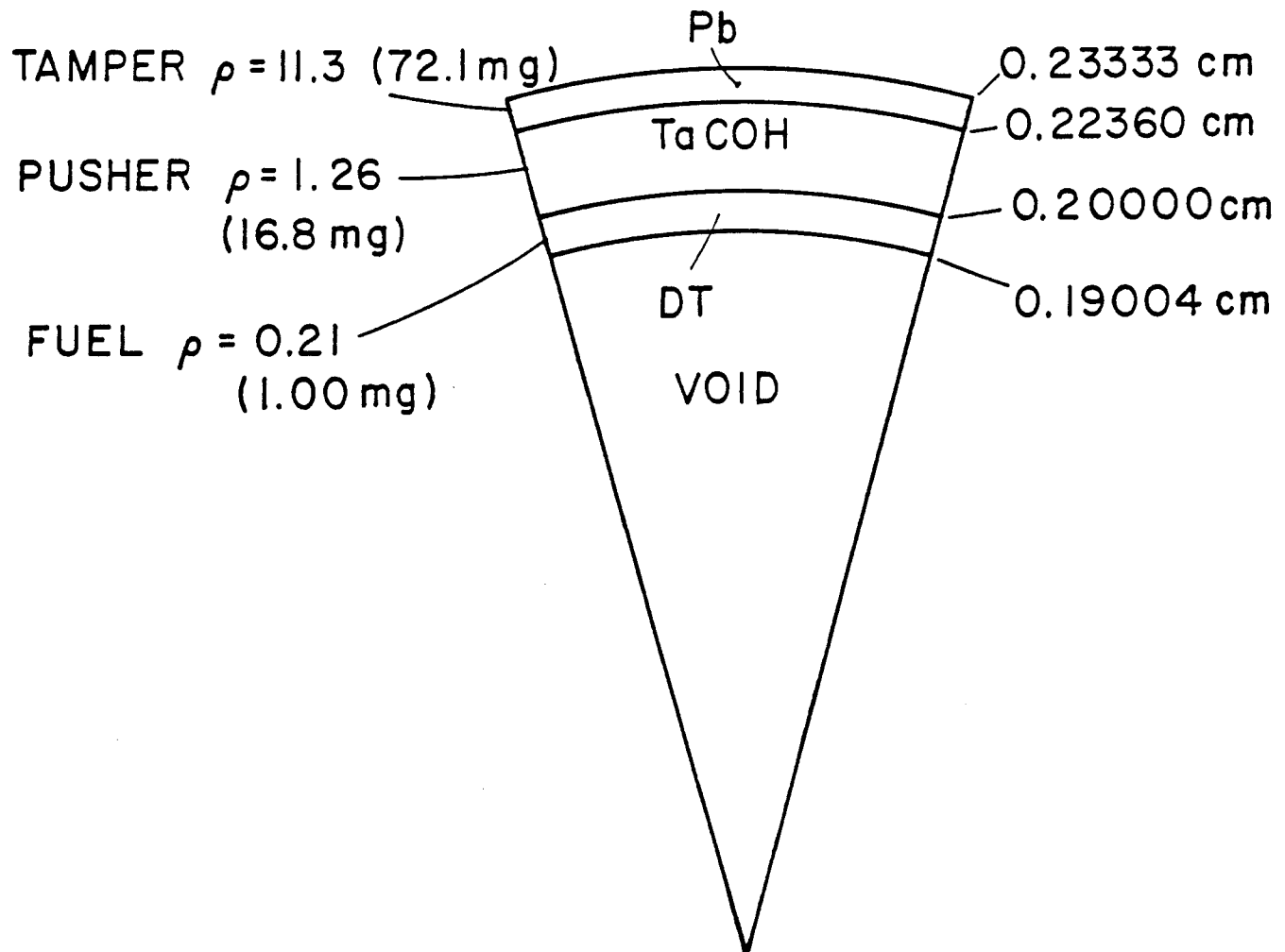
0.22360 cm

0.20000 cm

0.19004 cm

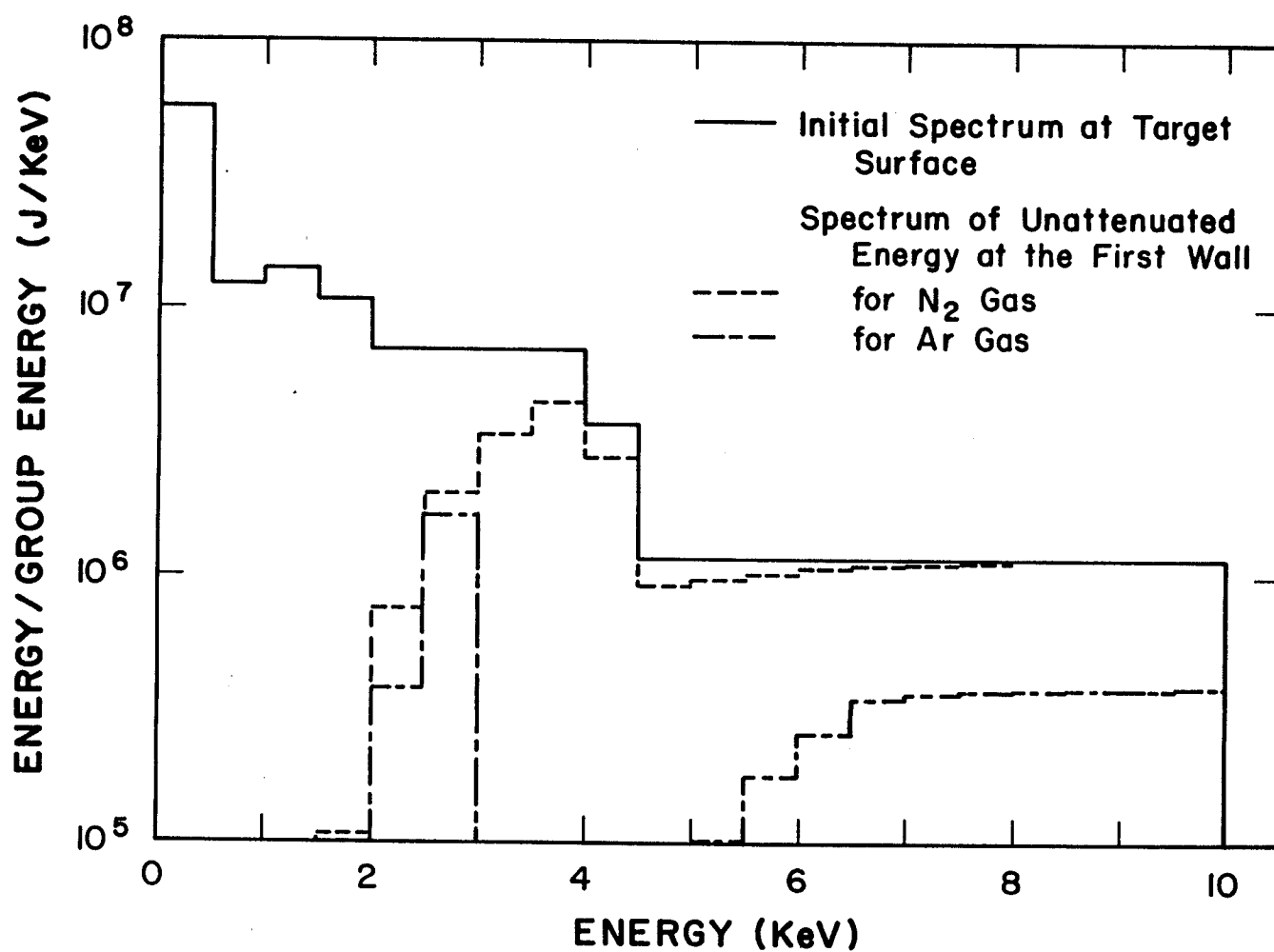Fig. 2. Target design used for generated output spectra.

Fig. 3. X-ray spectrum at the exploding target surface and at the first wall for N_2 and Ar gases at a density of 2.25×10^{-5} g/cm^3.

energy group. This group is strongly attenuated by the gas, thus character-
izing the short range of the ion debris. The initial pellet x-ray energy, the
energy deposited in the gas and the unattenuated energy reaching the first
wall are summarized in Table 3. Table 3 shows that more x-ray energy is
deposited in the higher Z Ar gas than in the N_2 gas and that more x-ray energy
is deposited as the mass density increases. The energy spectra of the x-rays
incident on the wall for the N_2 and Ar gases with a mass density of 2.25 x
10^{-5} g/cm^3 are shown in Fig. 3. The difference in these spectra is of course
due to the difference of atomic number of the gases.

The details of the microfireball behavior in the N_2 gas with a mass
density of 2.25 x 10^{-5} g/cm^3 (27.3 torr at 0°C) are given in Figs. 4 through
9. The hydrodynamic motion of the gas is shown in Fig. 4. The radii of the
Lagrangian zone boundaries are plotted against time, showing the propagation
of the shock front to the wall and reflection off of the wall. Figures 5, 6
and 7 are plots of the plasma temperature, the radiation temperature and the
plasma pressure profiles as a function of radius at different times. These
figures show that there is a small peak around the radius of 20 cm on the
profile at 1.80 x 10^{-7} ms. This unphysical behavior is attributable to over-
estimation of the x-ray bleaching effect in the region, R $\lesssim$ 20 cm. Hence, a
large amount of the pellet x-ray energy is absorbed around 20 cm. However,
the peak occurs only at very early times so that its effect on the fireball
behavior is negligible. Figure 8 is a plot of the heat flux and mechanical
overpressure experienced at the wall as a function of time. The radiation
energy reaches the wall in two distinct pulses. The largest instantaneous
heat flux, 485 kW/cm^2, occurs very early in time, 5.22 x 10^{-8} s, and the
second largest instantaneous heat flux, 3.78 kW/cm^2, occurs at almost the same

Table 3. Deposition of X-Ray Energy of 200 MJ Target Yield

at the Initial Condition (MJ)

Mass Density (g/cm^3)	Type of Energy	N_2	Ar
	Initial Energy	53.81	
4.17×10^{-5}	Deposited Energy	44.49	52.29
	Unattenuated Energy	9.32	1.52
2.25×10^{-5}	D.E.	41.28	50.25
	U.E.	12.53	3.56
1.33×10^{-5}	D.E.	38.25	47.45
	U.E.	15.56	6.36
8.33×10^{-6}	D.E.	35.52	44.07
	U.E.	18.29	9.74
4.12×10^{-6}	D.E.	31.41	37.87
	U.E.	22.40	15.94
2.50×10^{-6}	D.E.	28.19	
	U.E.	25.62	

Fig. 4. Hydrodynamic motion of Lagrangian zone boundaries plotted against time in the multifrequency model for a 200 MJ target yield in 27.3 torr (at 0°C), N_2 gas.

1	T=	.0000 MSEC
2	T=	.0103 MSEC
3	T=	.0544 MSEC
4	T=	.1809 MSEC
5	T=	.3966 MSEC
6	T=	.4900 MSEC
7	T=	.6937 MSEC

Fig. 5. Plasma temperature profiles at various times in the multifrequency model for a 200 MJ target yield in 27.3 torr (at 0°C), N_2 gas.

15

RADIATION TEMPERATURE

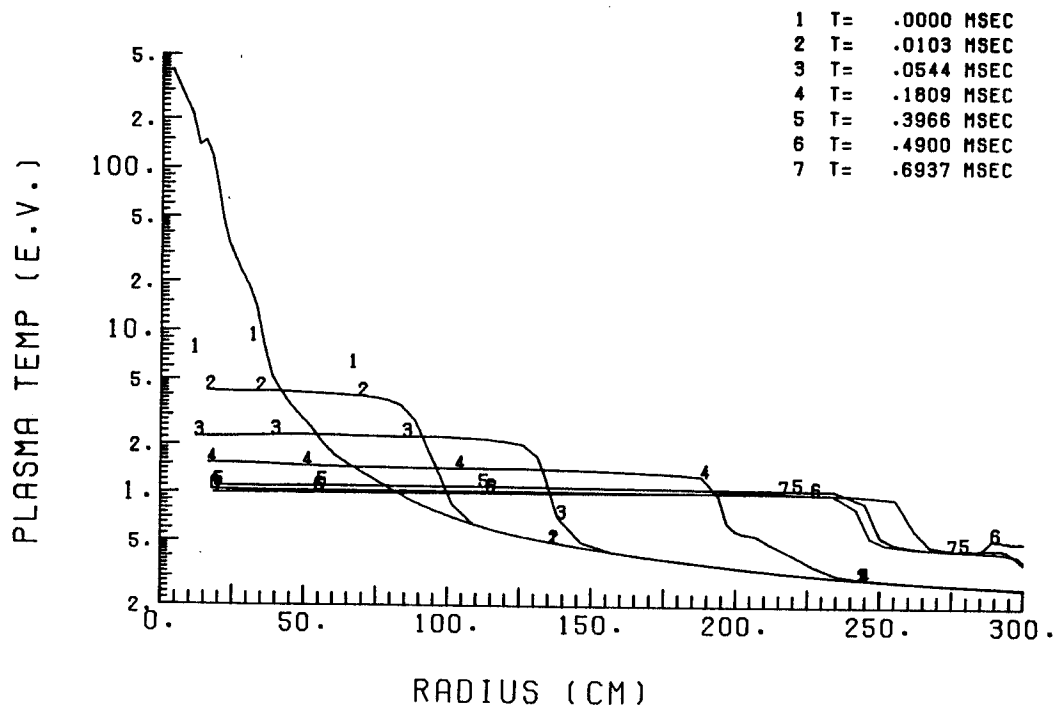|		
1	T=	.0000 MSEC
2	T=	.0103 MSEC
3	T=	.0544 MSEC
4	T=	.1809 MSEC
5	T=	.3966 MSEC
6	T=	.4900 MSEC
7	T=	.6937 MSEC

RADIATION TEMP (E.V.)

RADIUS (CM)

Fig. 6. Radiation temperature profiles at various times in the multifrequency model for a 200 MJ target yield in 27.3 torr (at 0°C), N_2 gas.

PLASMA PRESSURE

1	T=	.0000 MSEC
2	T=	.0103 MSEC
3	T=	.0544 MSEC
4	T=	.1809 MSEC
5	T=	.3966 MSEC
6	T=	.4900 MSEC
7	T=	.6937 MSEC

PLASMA PRESS (ATM)

RADIUS (CM)

Fig. 7. Plasma pressure profiles at various times in the multifrequency model for a 200 MJ target yield in 27.3 torr (at 0°C), N_2 gas.
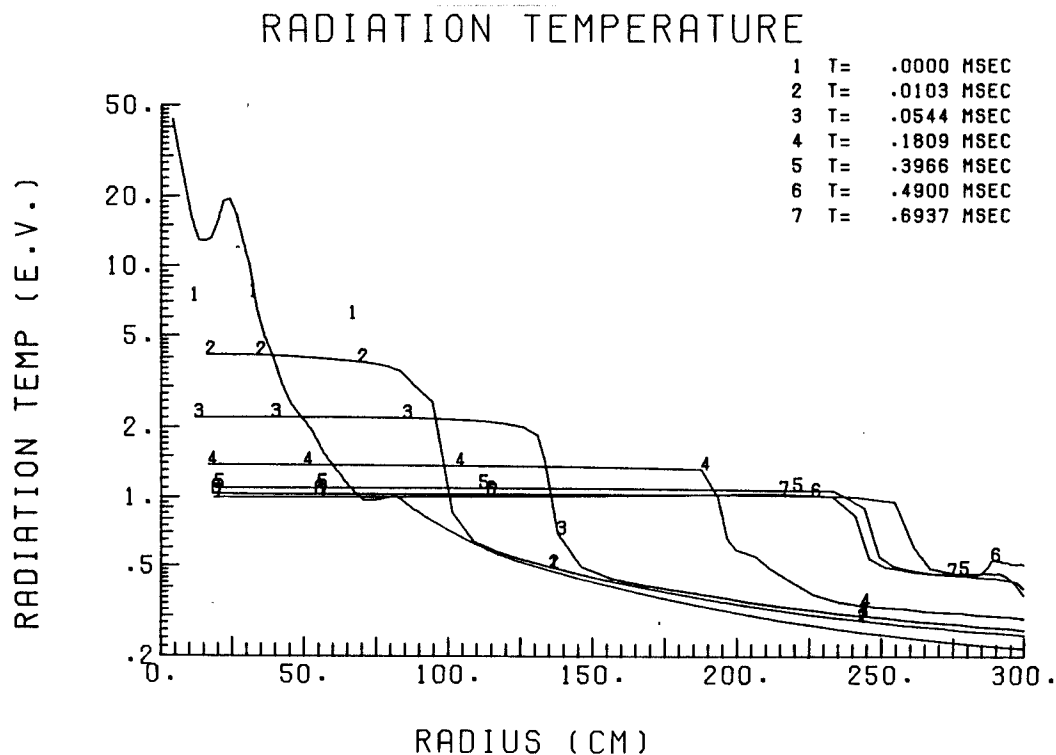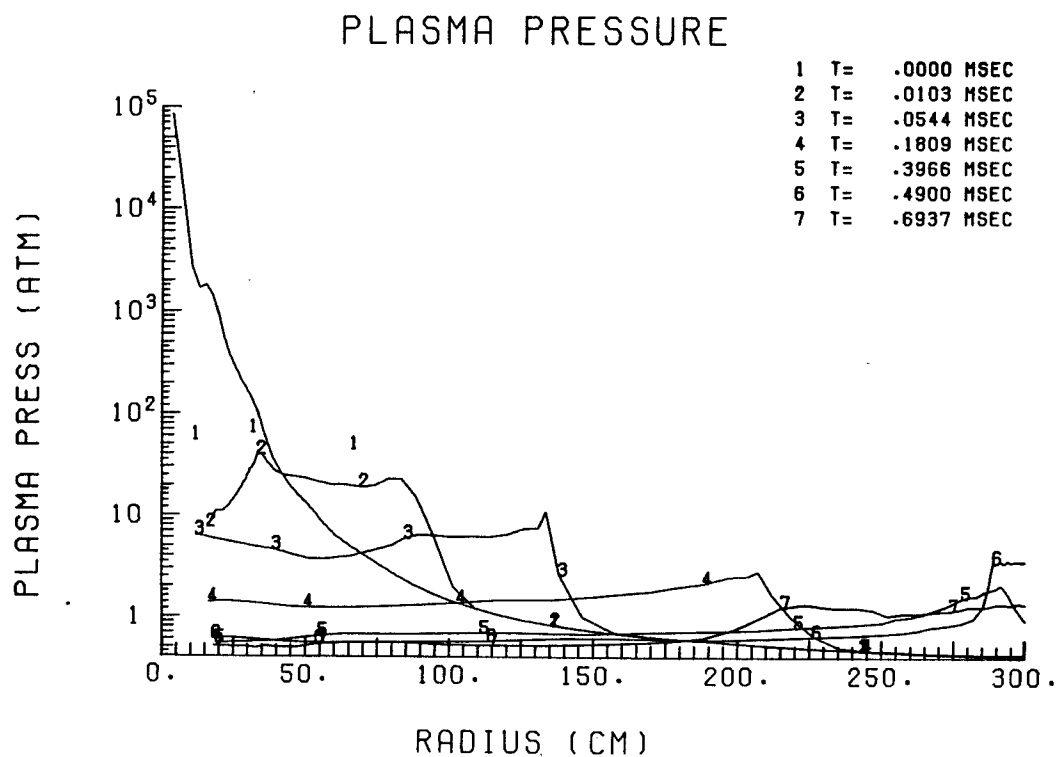
16

PRESSURE AND HEAT FLUX AT FIRST WALL

FLPEAK = .4621-003 KJ/CM**2
FLTOTAL = .1254-002 KJ/CM**2
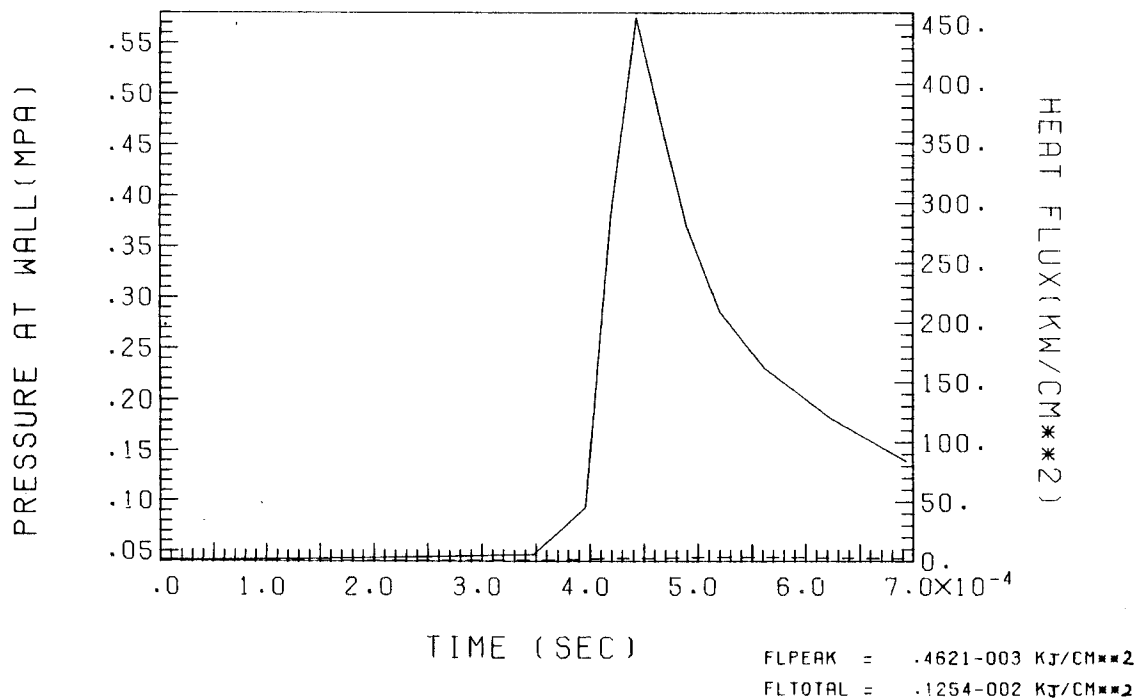
Fig. 8. Overpressure and heat flux at a 3 meter radius first wall in the multifrequency model for a 200 MJ target yield in 27.3 torr (at 0°C), N_2 gas.
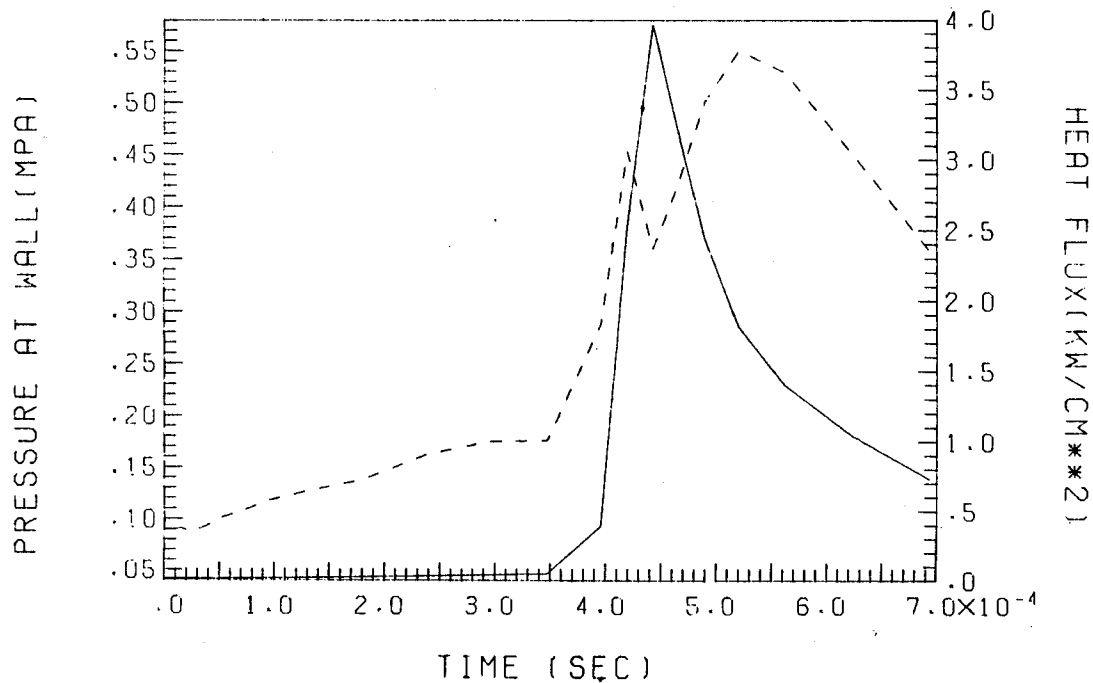
PRESSURE AND HEAT FLUX AT FIRST WALL

Fig. 9. Overpressure and expansion of the second pulse of heat flux at a 3 meter radius first wall in the multifrequency model for a 200 MJ target yield in 27.3 torr (at 0°C), N_2 gas.

17

time when the wall experiences the maximum overpressure of 0.624 MPa. An expanded plot of the second pulse in time is shown in Fig. 9. Although the peak heat flux of the first pulse is much larger, its pulse width, 0.31 μs, is much smaller than that of the second pulse, 450 μs. The fireball behavior of the same case obtained by the two-temperature model is shown in Figs. 10 through 14. The hydrodynamic behavior of the N_2 gas in the two-temperature model is similar to that in the multifrequency model. For example, the maximum overpressure at the wall, 0.679 MPa and its time, 0.420 ms, in the two-temperature model are very close to those, 0.624 MPa and 0.433 ms, in the multifrequency model. However, Fig. 14 shows that there is only one pulse of radiation predicted by the two-temperature model. The peak heat flux, 9.34 kW/cm^2, occurs simultaneously with the maximum overpressure and its pulse width is ~ 400 μs.

The fireball behavior in the Ar gas with the same mass density (10 torr at 0°C) in the multifrequency model and the two-temperature model are shown in Figs. 15 through 24. The hydrodynamic behavior of the Ar gas in the two-temperature model is very different from that in the multifrequency model. For example, the maximum overpressure at the wall and its time are 0.177 MPa and 0.256 ms in the two-temperature model, while they are 0.227 MPa and 0.504 ms in the multifrequency model. The radiation transport is also very different between the two models. The multifrequency model predicts only one early pulse of radiation with the peak heat flux at the wall, 3300 kW/cm^2, its time 4.58 x 10^{-8} s, and the pulse width, ~ 10 μs. However, the corresponding values in the two-temperature model are 138 kW/cm^2, 2.45 x 10^{-4} s and ~ 500 μs and the peak heat flux occurs simultaneously with the maximum overpressure at the wall.
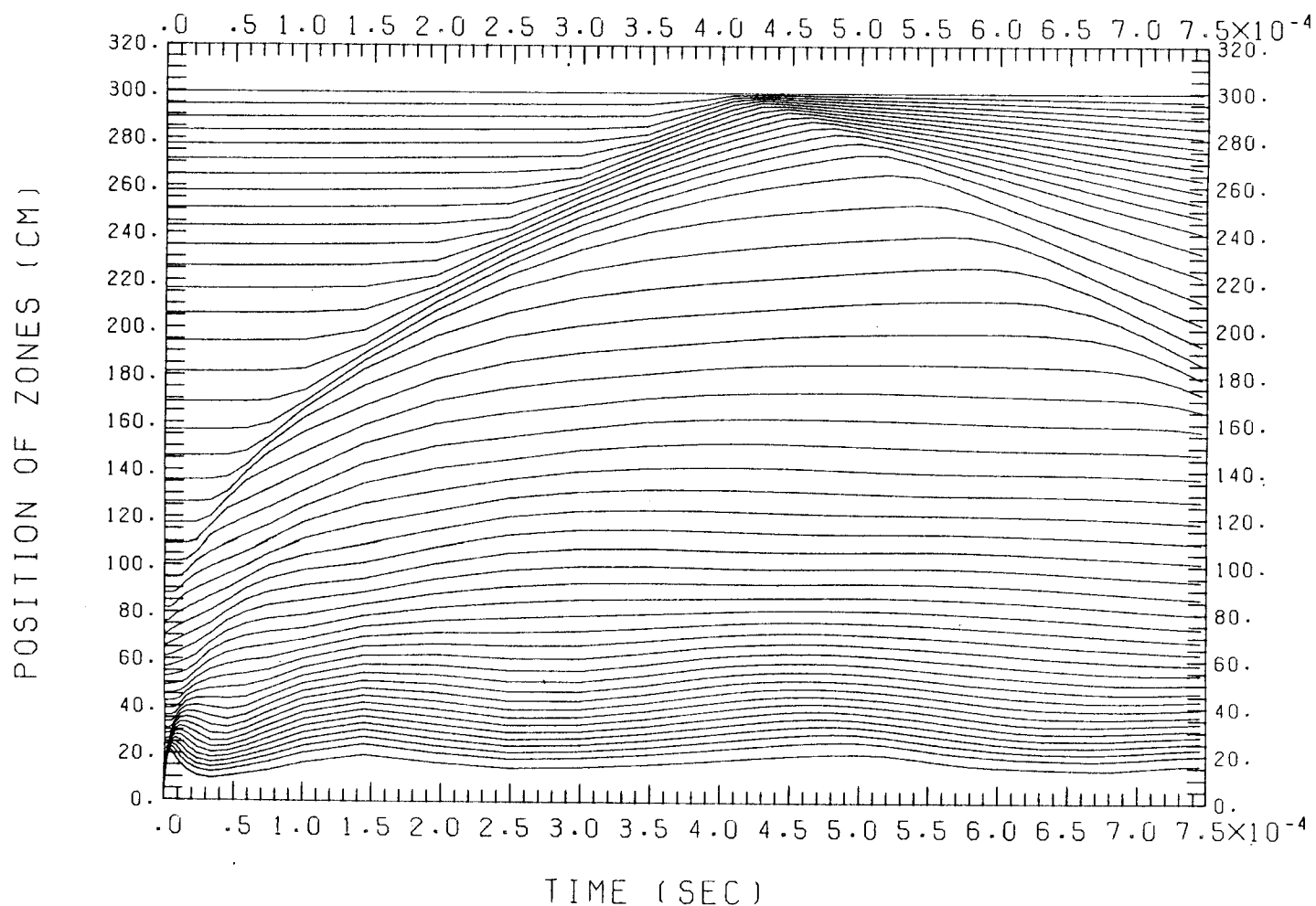
WORLD LINES FOR ZONES

Fig. 10. Hydrodynamic motion of Lagrangian zone boundaries plotted against time in the two-temperature model for a 200 MJ (target yield in 27.3 torr (at 0°C), N_2 gas.

PLASMA TEMPERATURE

1	T=	.1800-06 MSEC
2	T=	.1676-01 MSEC
3	T=	.5977-01 MSEC
4	T=	.1956+00 MSEC
5	T=	.3897+00 MSEC
6	T=	.4641+00 MSEC
7	T=	.5419+00 MSEC

Fig. 11. Plasma temperature profiles at various times in the two-temperature model for a 200 MJ target yield in 27.3 torr (at 0°C), N_2 gas.

RADIATION TEMPERATURE

1	T=	.1800-06 MSEC
2	T=	.1676-01 MSEC
3	T=	.5977-01 MSEC
4	T=	.1956+00 MSEC
5	T=	.3897+00 MSEC
6	T=	.4641+00 MSEC
7	T=	.5419+00 MSEC

Fig. 12. Radiation temperature profiles at various times in the two-temperature model for a 200 MJ target yield in 27.3 torr (at 0°C), N_2 gas.

20

PLASMA PRESSURE

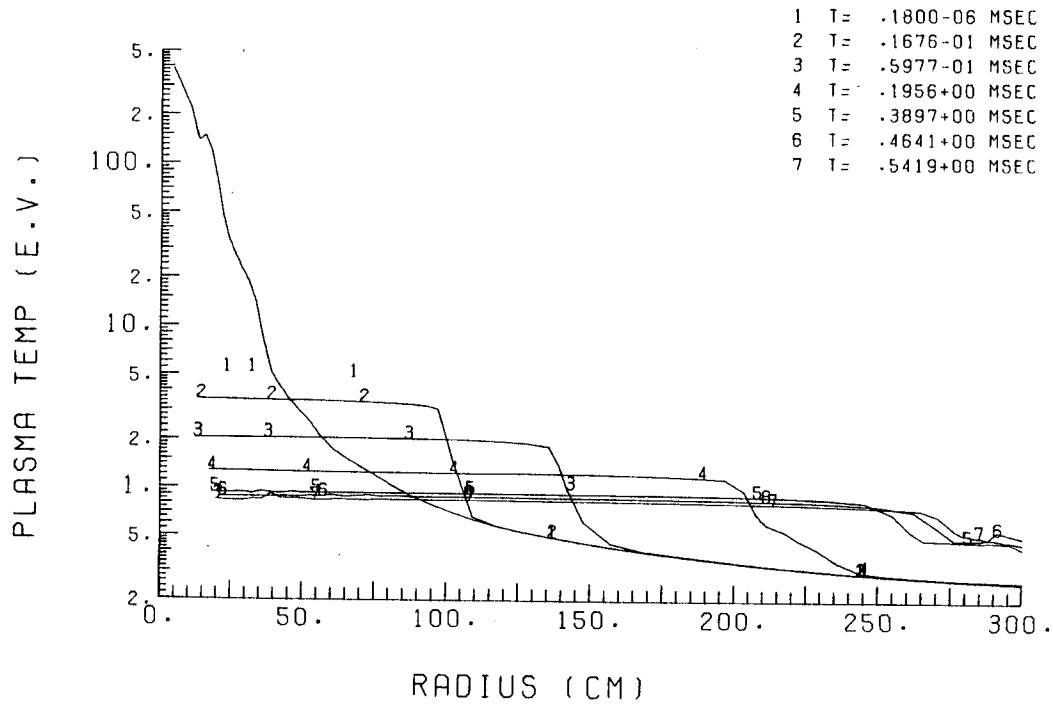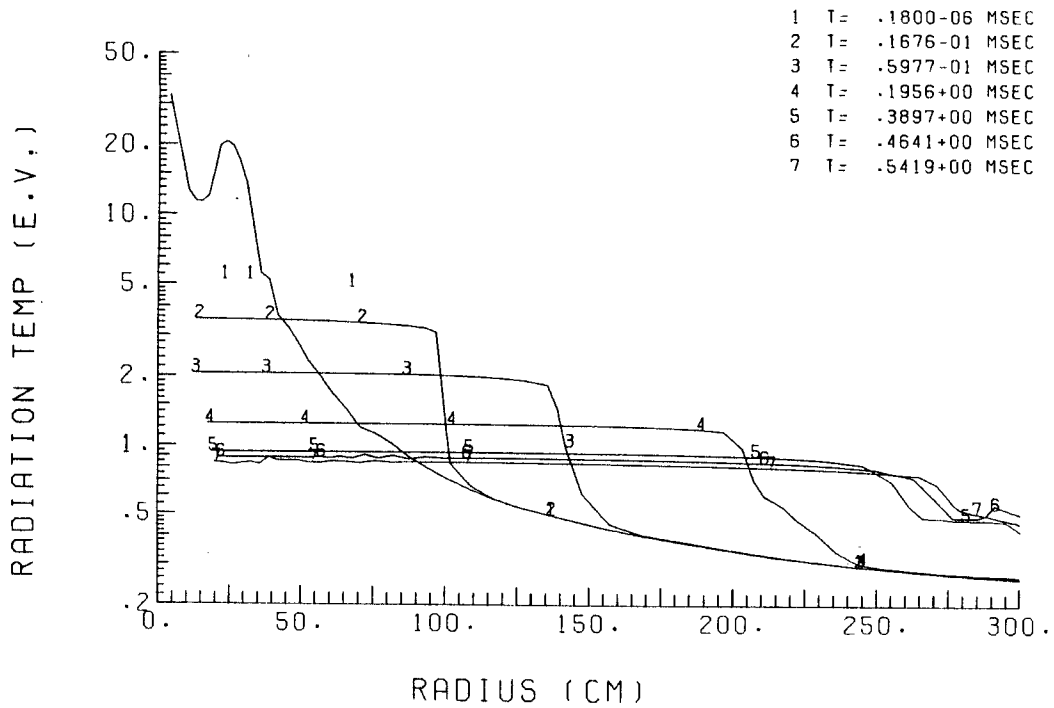| 1	T=	.1800-06	MSEC
2	T=	.1676-01	MSEC
3	T=	.5977-01	MSEC
4	T=	.1956+00	MSEC
5	T=	.3897+00	MSEC
6	T=	.4641+00	MSEC
7	T=	.5419+00	MSEC

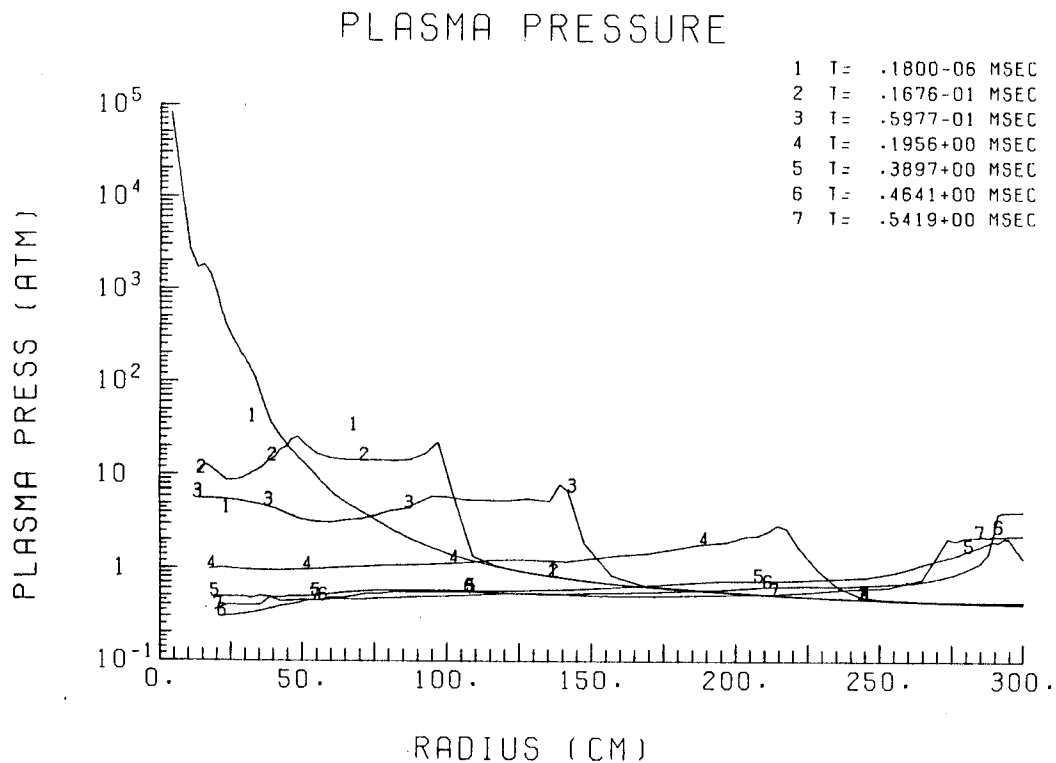Fig. 13. Plasma pressure profiles at various times in the two-temperature model for a 200 MJ target yield in 27.3 torr (at 0°C), N_2 gas.

PRESSURE AND HEAT FLUX AT FIRST WALL

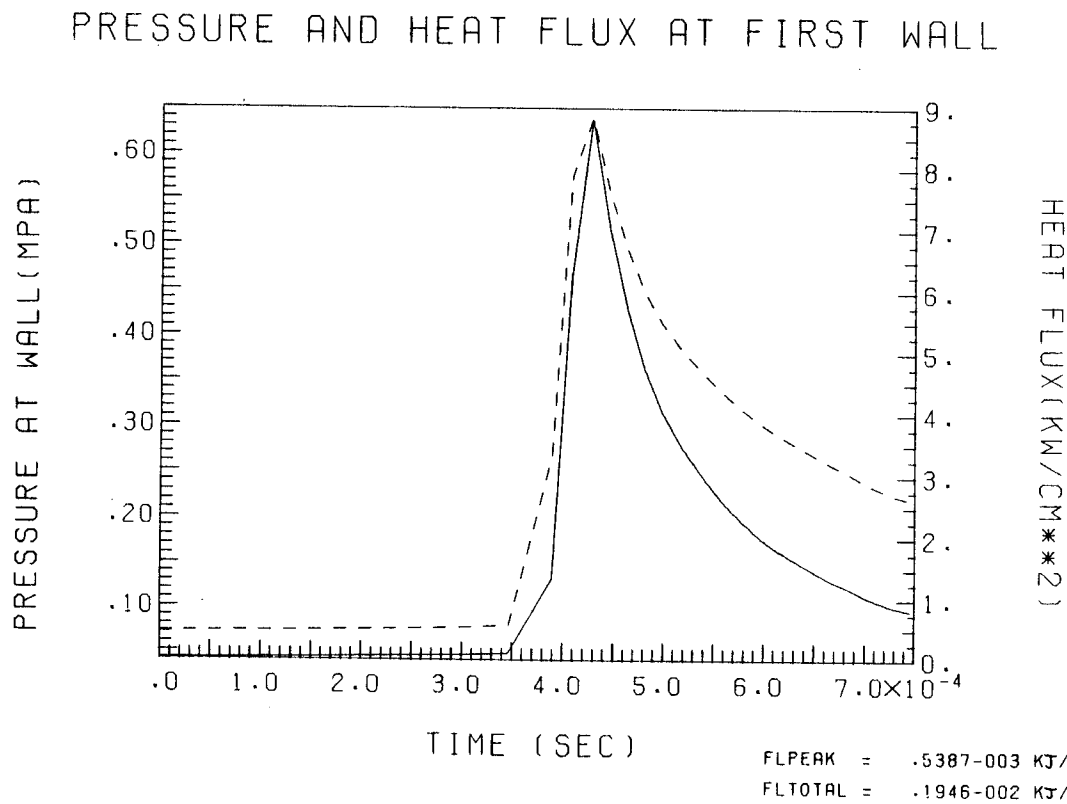

FLPEAK = .5387-003 KJ/CM**2
FLTOTAL = .1946-002 KJ/CM**2

Fig. 14. Overpressure and heat flux at a 3 meter radius first wall in the two-temperature model for a 200 MJ target yield in 27.3 torr (at 0°C), N_2 gas.
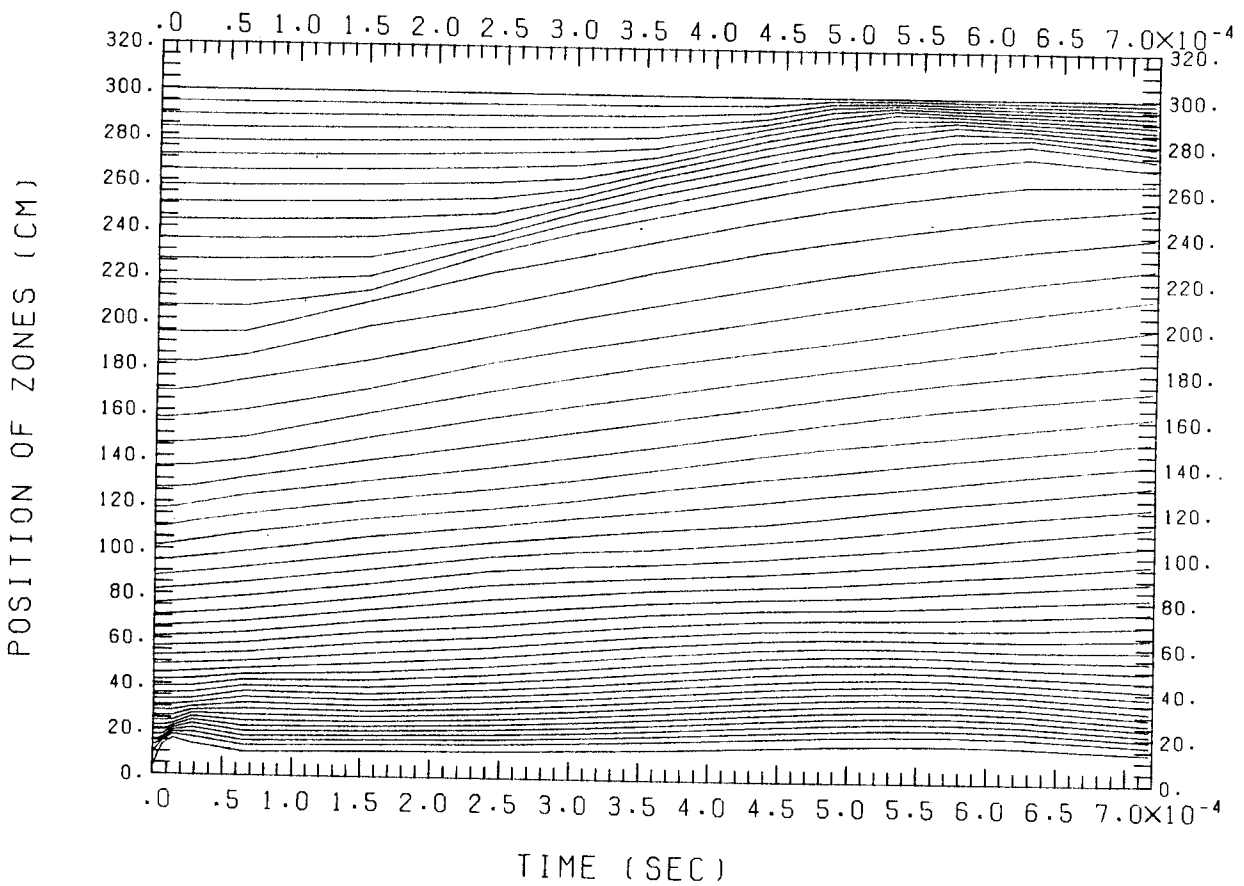
21

Fig. 15. Hydrodynamic motion of Lagrangian zone boundaries plotted against time in the multifrequency model for a 200 MJ target yield in 10.0 torr (at 0°C), Ar gas.
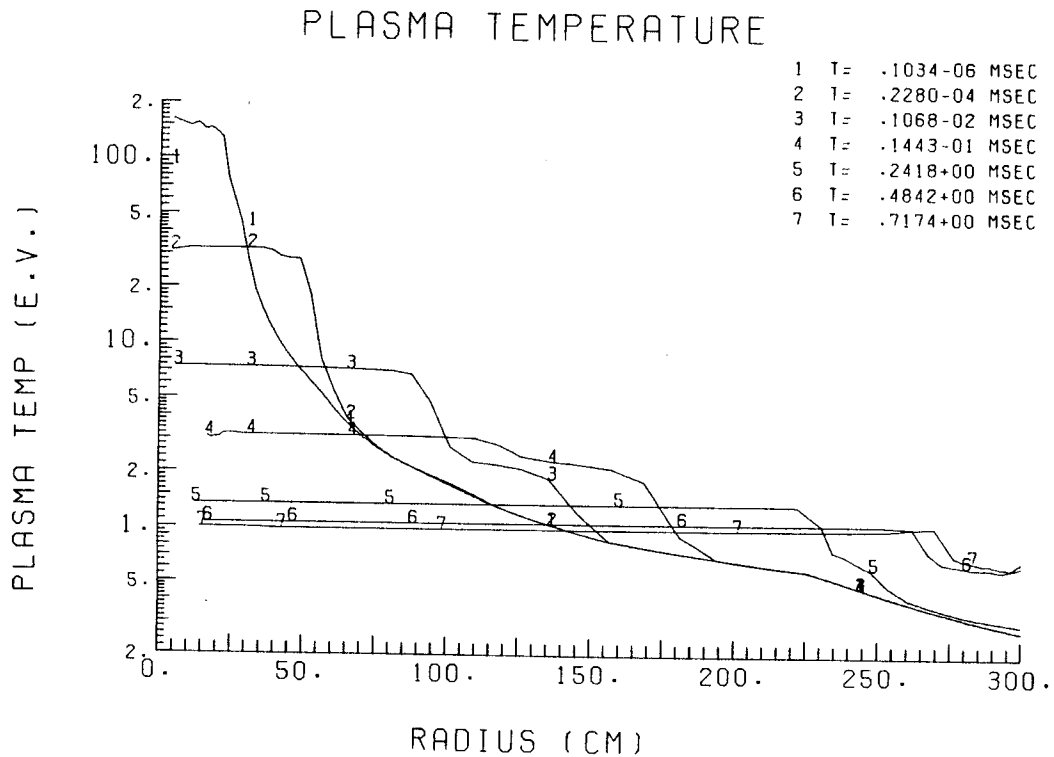

Fig. 16. Plasma temperature profiles at various times in the multifrequency model for a 200 MJ target yield in 10.0 torr (at 0°C), Ar gas.
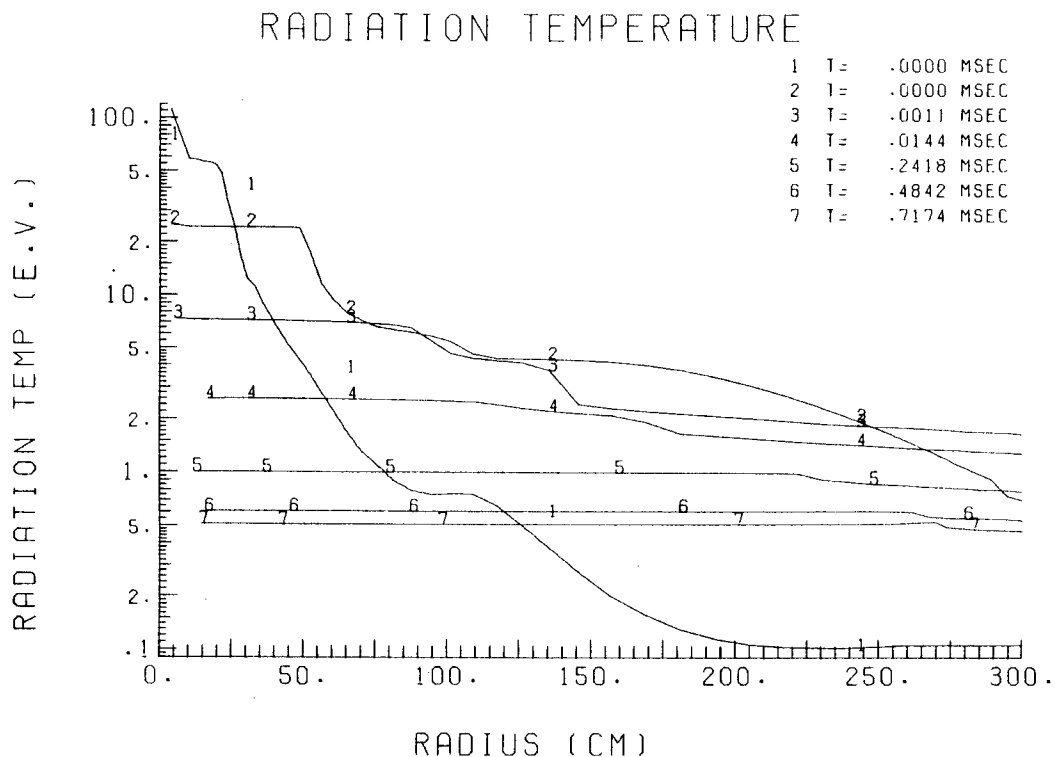
RADIATION TEMPERATURE

1	T =	.0000 MSEC
2	T =	.0000 MSEC
3	T =	.0011 MSEC
4	T =	.0144 MSEC
5	T =	.2418 MSEC
6	T =	.4842 MSEC
7	T =	.7174 MSEC

RADIATION TEMP (E.V.)

RADIUS (CM)

Fig. 17. Radiation temperature profiles at various times in the multifrequency model for a 200 MJ target yield in 10.0 torr (at 0°C), Ar gas.

PLASMA PRESSURE

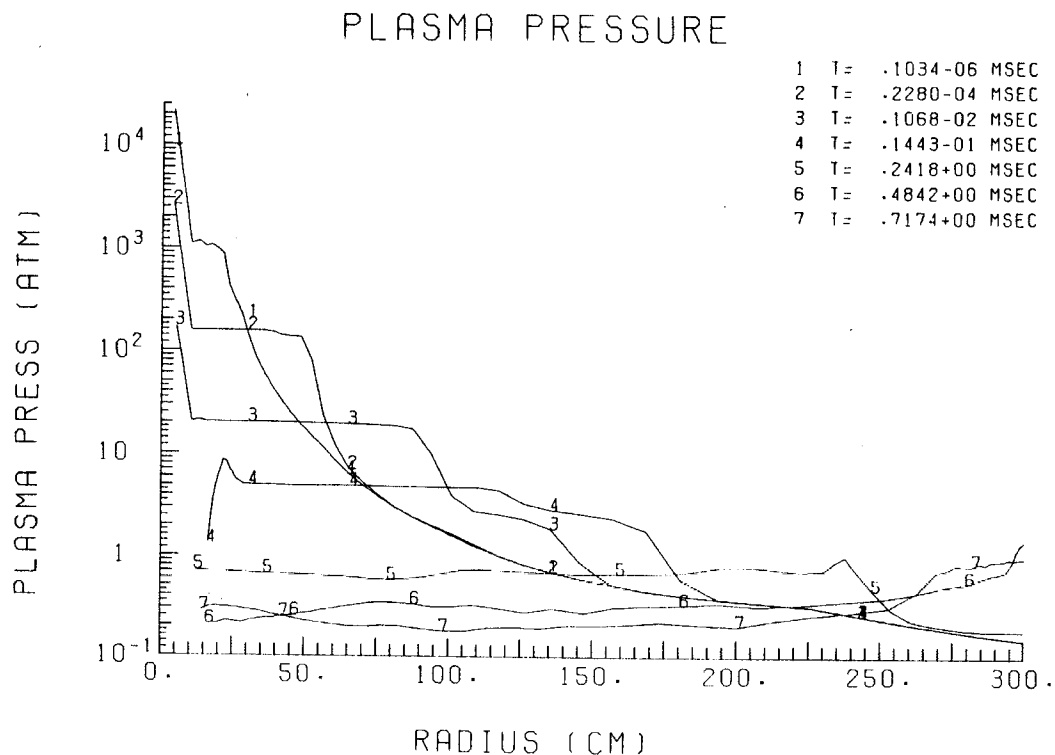|		
1	T =	.1034-06 MSEC
2	T =	.2280-04 MSEC
3	T =	.1068-02 MSEC
4	T =	.1443-01 MSEC
5	T =	.2418+00 MSEC
6	T =	.4842+00 MSEC
7	T =	.7174+00 MSEC

PLASMA PRESS (ATM)

RADIUS (CM)

Fig. 18. Plasma pressure profiles at various times in the multifrequency model for a 200 MJ target yield in 10.0 torr (at 0°C), Ar gas.

23

PRESSURE AND HEAT FLUX AT FIRST WALL

FLPEAK = .3046-001 KJ/CM**
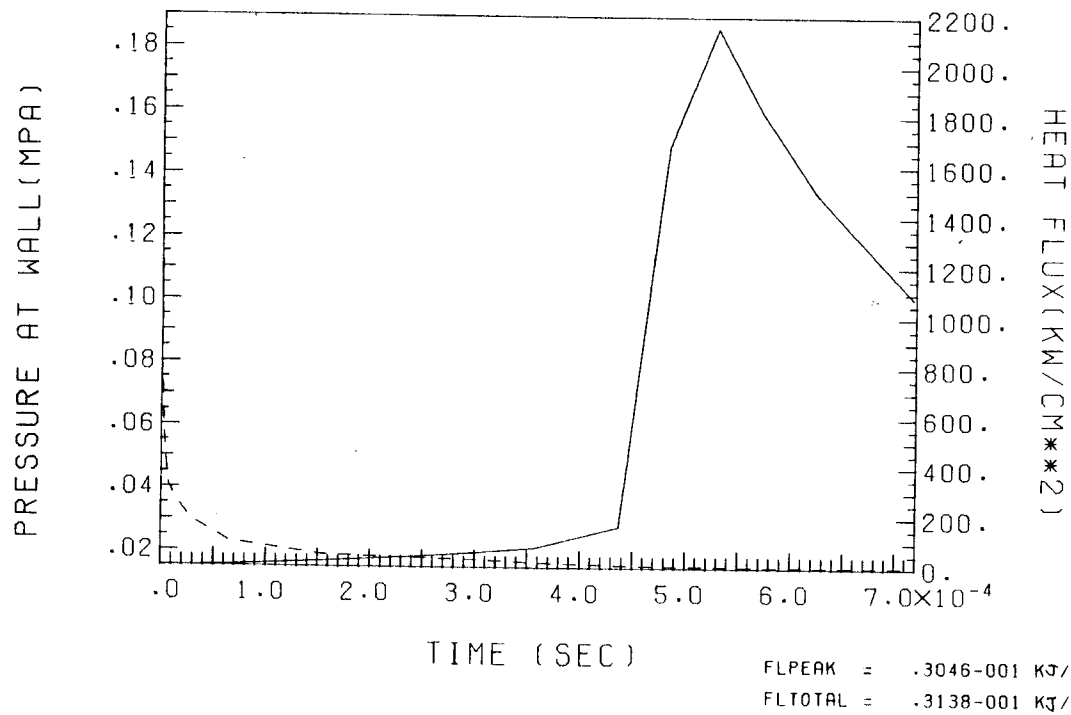FLTOTAL = .3138-001 KJ/CM**

Fig. 19. Overpressure and heat flux at a 3 meter radius first wall in the multifrequency model for a 200 MJ target yield in 10.0 torr (at 0°C), Ar gas.
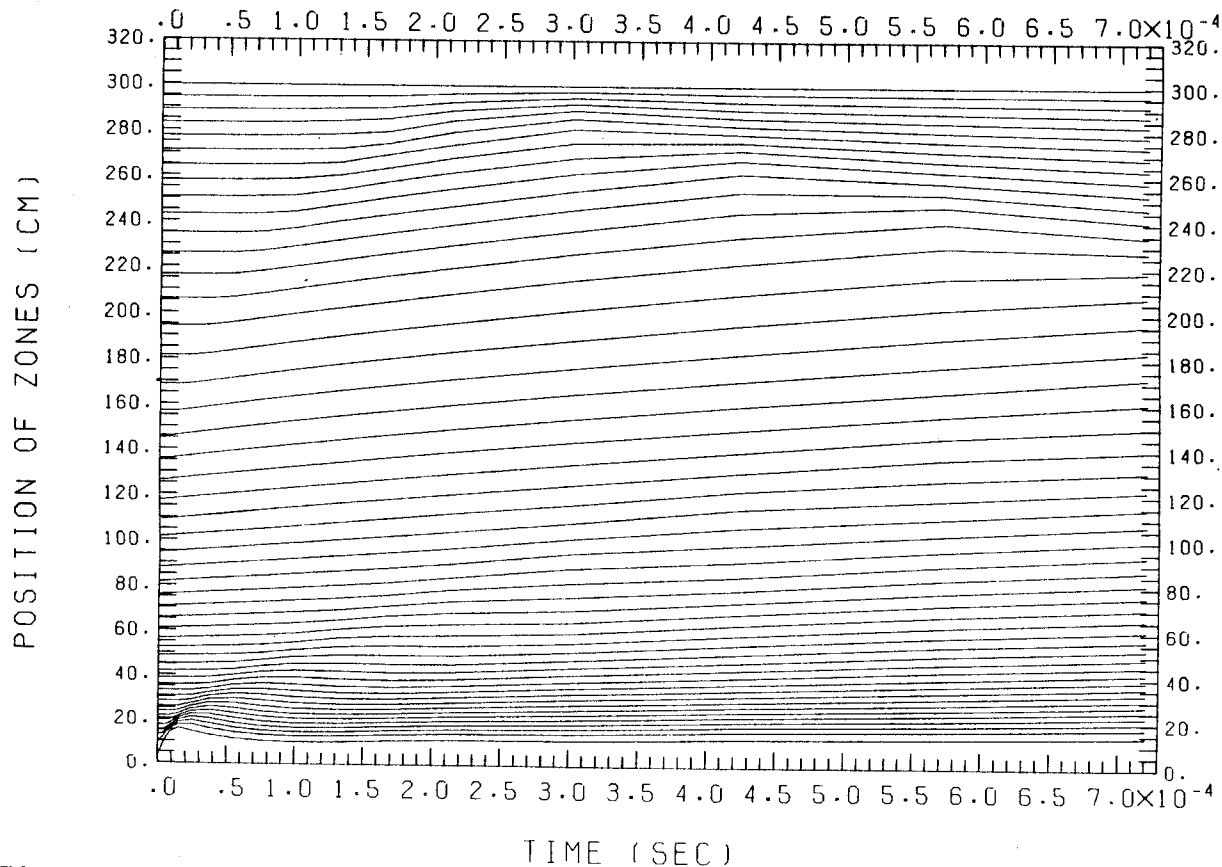

Fig. 20. Hydrodynamic motion of Lagrangian zone boundaries plotted against time in the two-temperature model for a 200 MJ target yield in 10.0 torr (at 0°C), Ar gas.
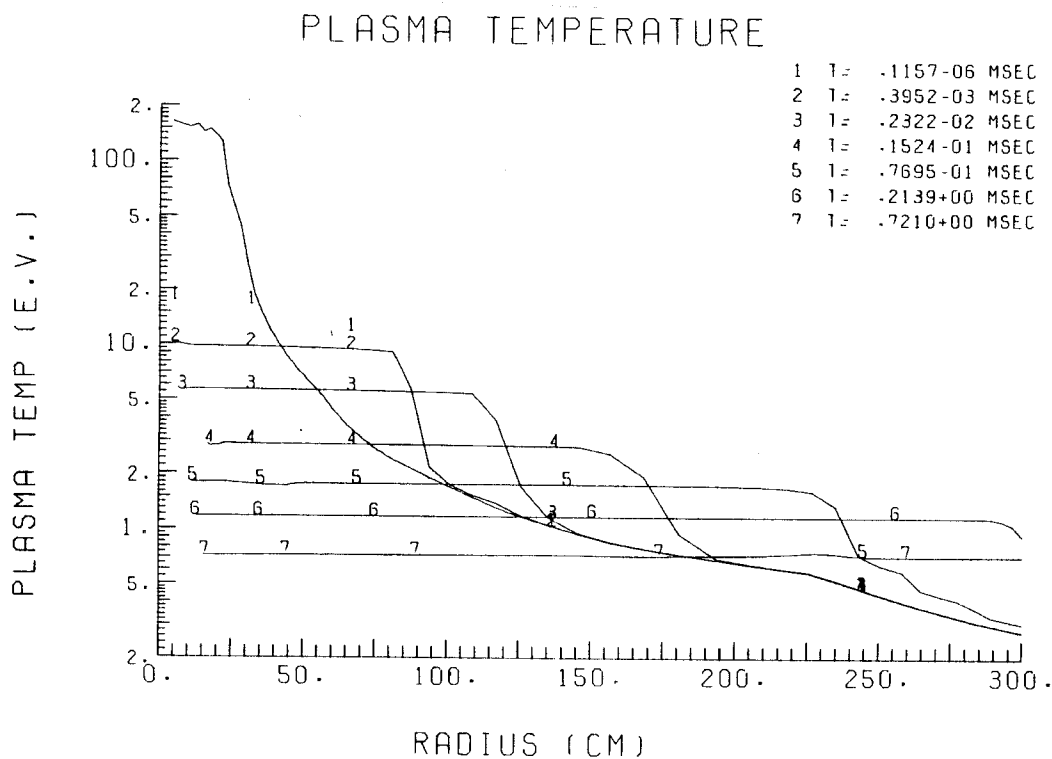
PLASMA TEMPERATURE

1	T=	.1157-06 MSEC
2	T=	.3952-03 MSEC
3	T=	.2322-02 MSEC
4	T=	.1524-01 MSEC
5	T=	.7695-01 MSEC
6	T=	.2139+00 MSEC
7	T=	.7210+00 MSEC

Fig. 21. Plasma temperature profiles at various times in the two-temperature model for a 200 MJ target yield in 10.0 torr (at 0°C), Ar gas.

RADIATION TEMPERATURE

|		
1	T=	.1157-06 MSEC
2	T=	.3952-03 MSEC
3	T=	.2322-02 MSEC
4	T=	.1524-01 MSEC
5	T=	.7695-01 MSEC
6	T=	.2139+00 MSEC
7	T=	.7210+00 MSEC

Fig. 22. Radiation temperature profiles at various times in the two-temperature model for a 200 MJ target yield in 10.0 torr (at 0°C), Ar gas.
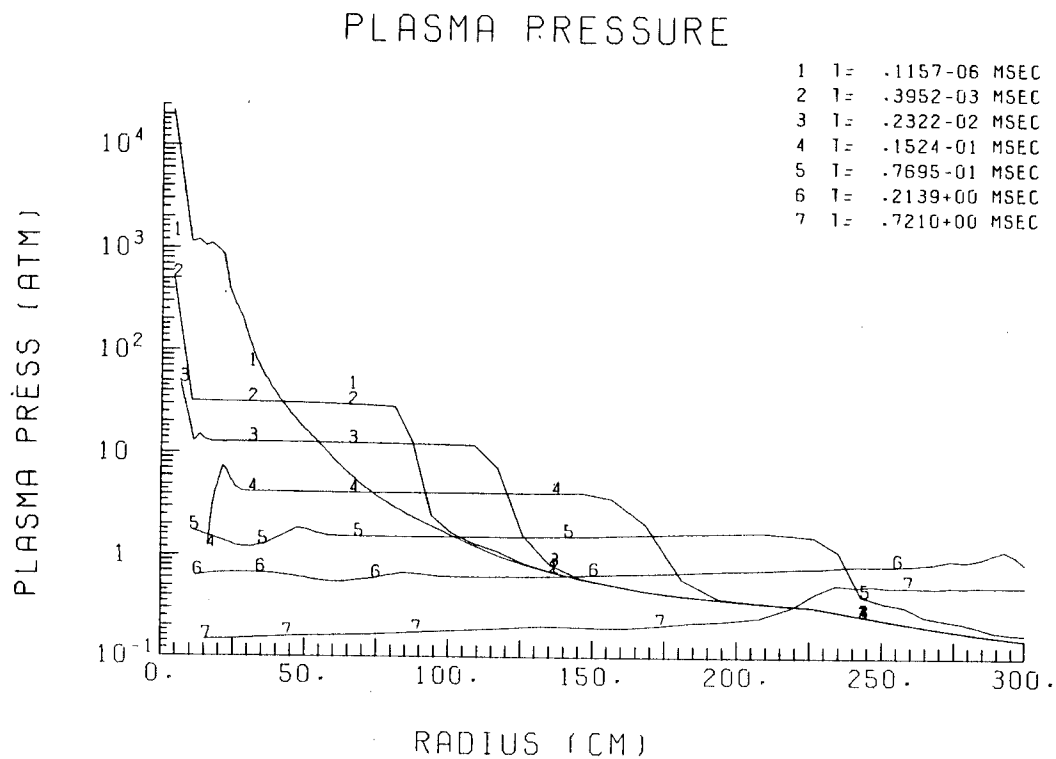
25

PLASMA PRESSURE

1	T=	.1157-06 MSEC
2	T=	.3952-03 MSEC
3	T=	.2322-02 MSEC
4	T=	.1524-01 MSEC
5	T=	.7695-01 MSEC
6	T=	.2139+00 MSEC
7	T=	.7210+00 MSEC

Fig. 23. Plasma pressure profiles at various times in the two-temperature model for a 200 MJ target yield in 10.0 torr (at 0°C), Ar gas.

PRESSURE AND HEAT FLUX AT FIRST WALL

FLPEAK = .1509-001 KJ/CM**2

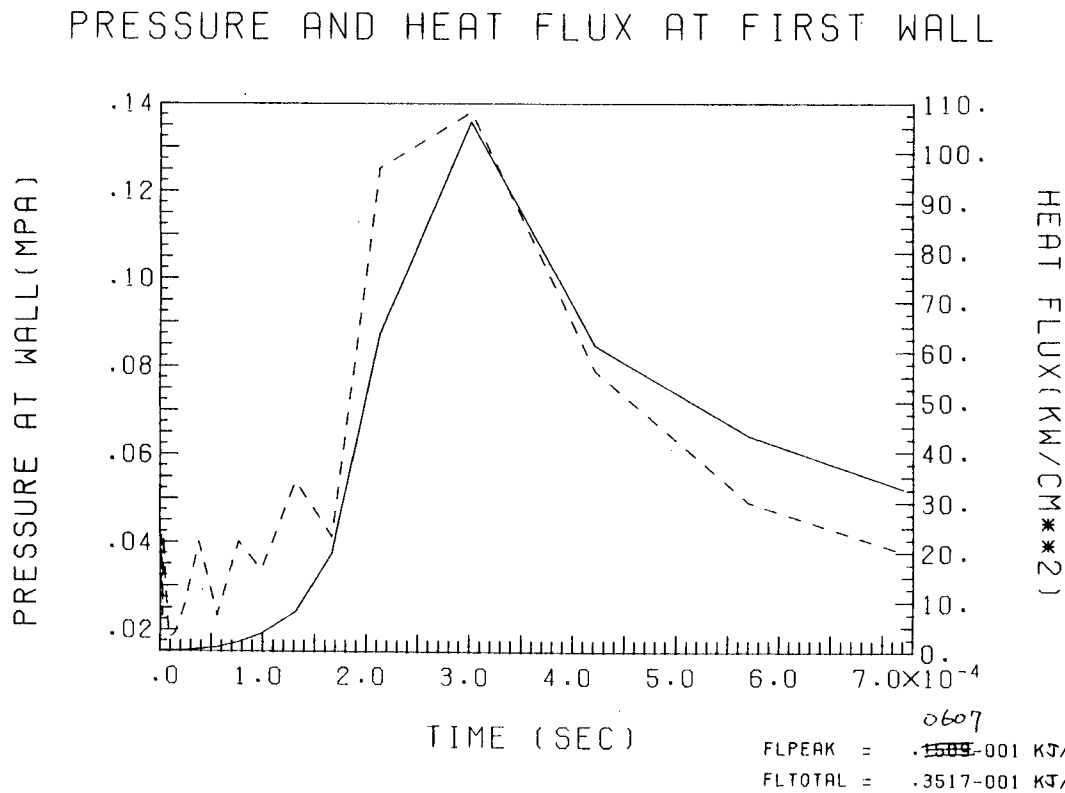FLTOTAL = .3517-001 KJ/CM**2
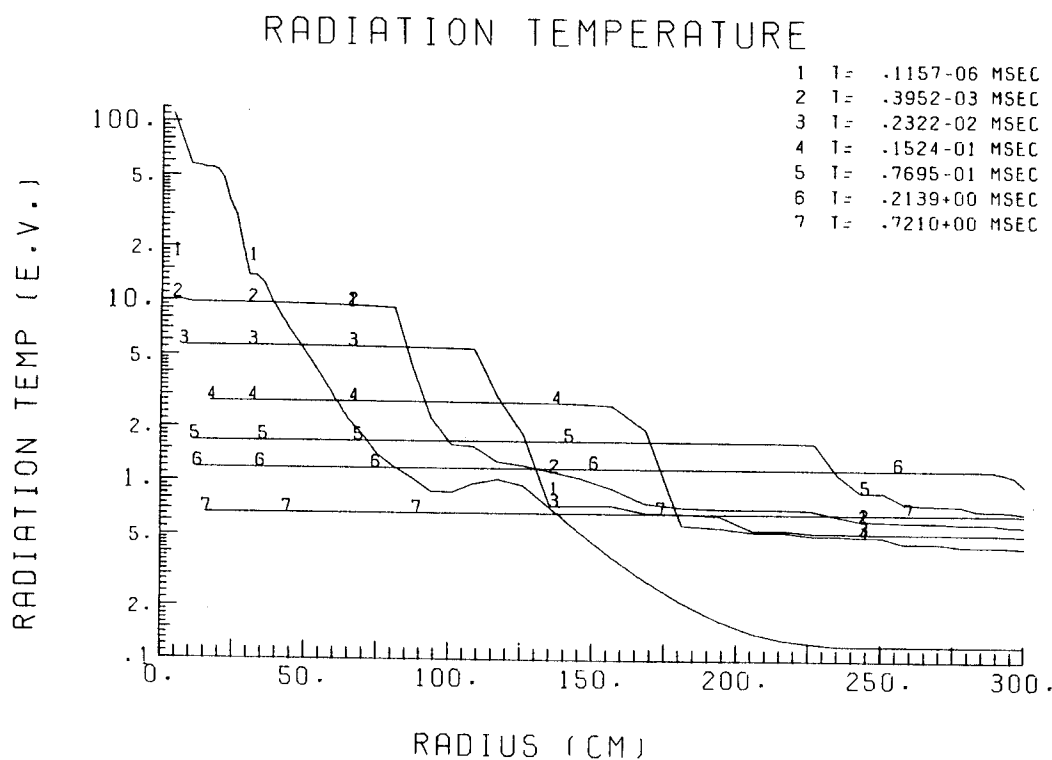
Fig. 24. Overpressure and heat flux at a 3 meter radius first wall in the two-temperature model for a 200 MJ target yield in 10.0 torr (at 0°C), Ar gas.

26

We have obtained the same information for N_2 and Ar gases for all of the mass densities given in Table 2. The integrated energy density radiated to the wall up to the time of the maximum overpressure and to a time following the shock reflection from the first wall are given in Figs. 25 and 26. The maximum pressure and its time as a function of mass density are shown in Figs. 27 and 28. Solid and dotted lines represent the results obtained by the multifrequency model and the two-temperature model, respectively. The energies radiated to the wall up to the time of the maximum pressure in the N_2 gas are the same for the two models. However, the two-temperature model predicts a much larger radiated energy after the arrival of the shock at the wall for gas densities below 4.12×10^{-6} g/cm^3 (5 torr at 0°C). Figures 27 and 28 show that the hydrodynamic behavior of the N_2 gas is the same for the two models for this range of the mass density.

In the cases of the Ar gas, a large amount of energy is radiated to the wall very early in time (~ 10 μs) in the multifrequency model while a large amount of energy is radiated to the wall after the maximum overpressure in the two-temperature model as shown in Figs. 25 and 26. Additionally, the total radiated energy in the two-temperature model is larger than that in the multi-frequency model. However, the calculation is stopped just after the shock wave reflects from the wall because we do not believe that the one-dimensional code accurately treats the inward directed reflected shock wave. The time of the calculation is smaller for smaller mass density cases since the shock wave arrives at the wall at an earlier time so that there is less time for the plasma to emit radiation and to cool. Therefore, the fact that the energy radiated to the wall decreases with decreasing mass density is an artifact of
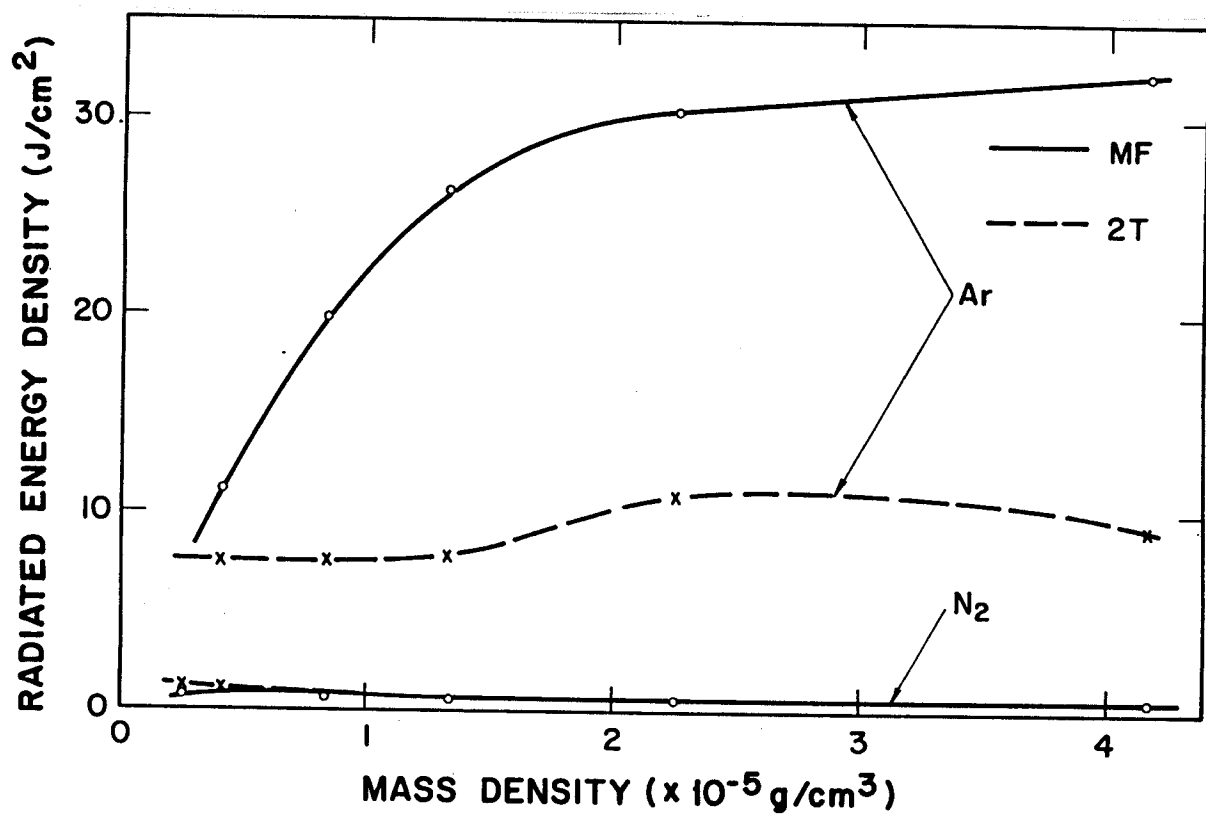
Fig. 25. Radiated energy density at a 3 meter radius first wall integrated up to the time of the maximum overpressure for a 200 MJ target yield.
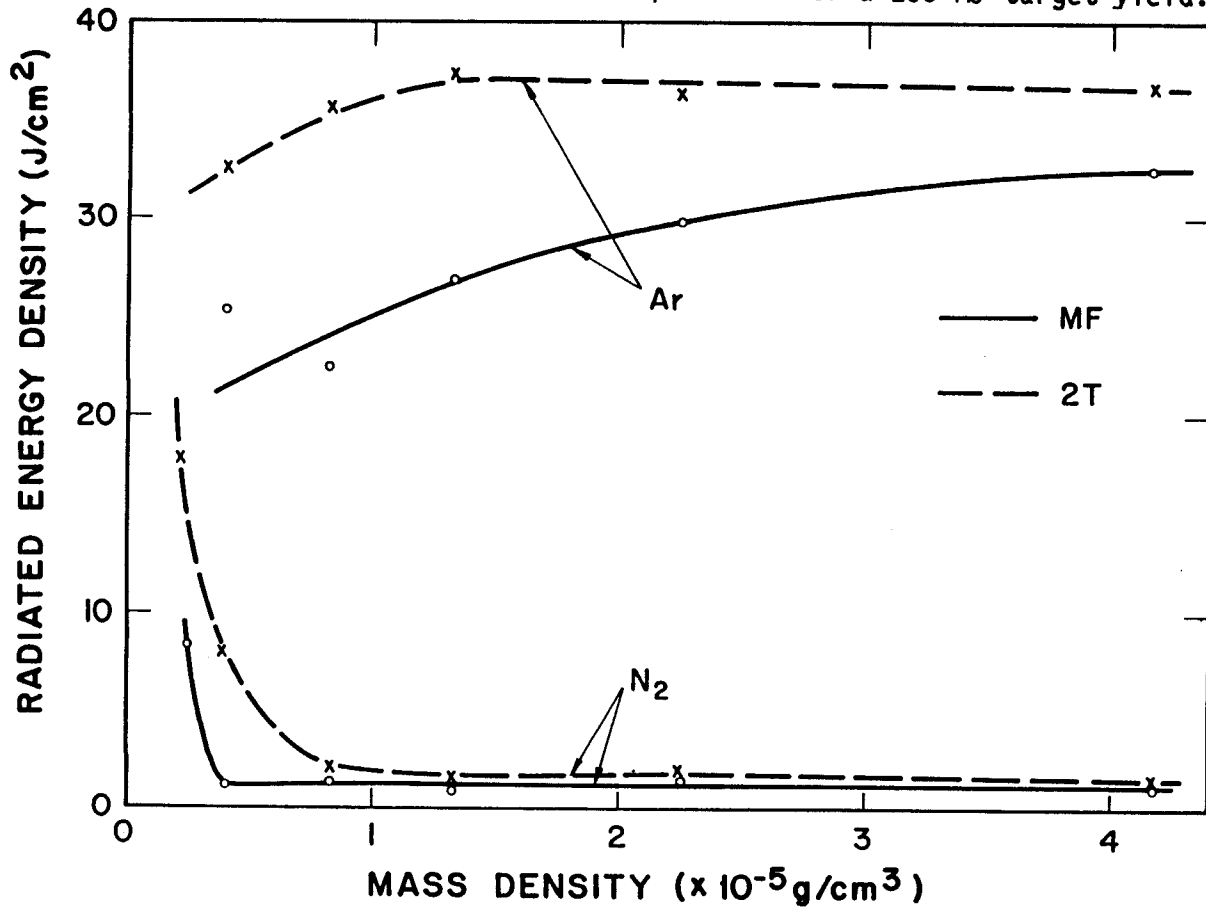

Fig. 26. Radiated energy density at a 3 meter radius first wall integrated up to a time following the shock reflection from the wall for a 200 MJ target yield.
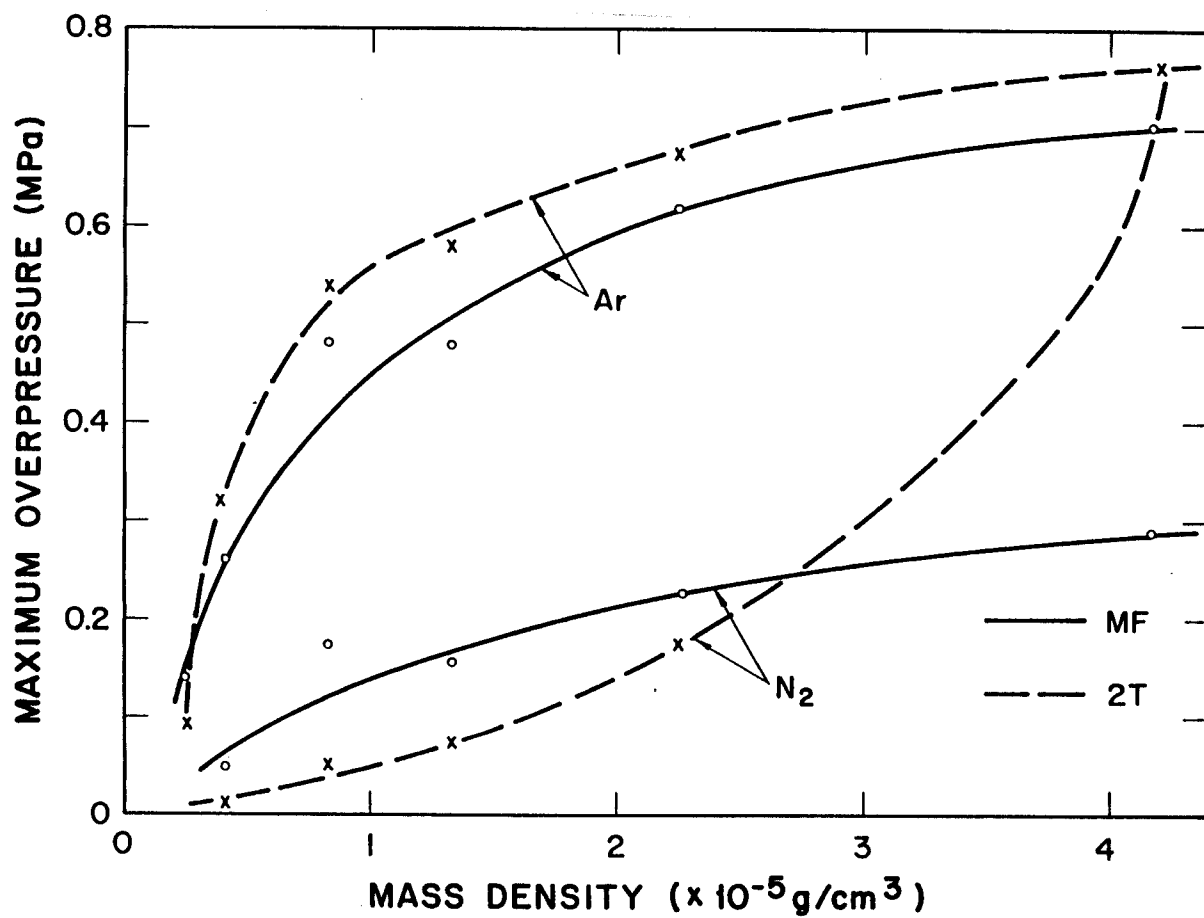
28

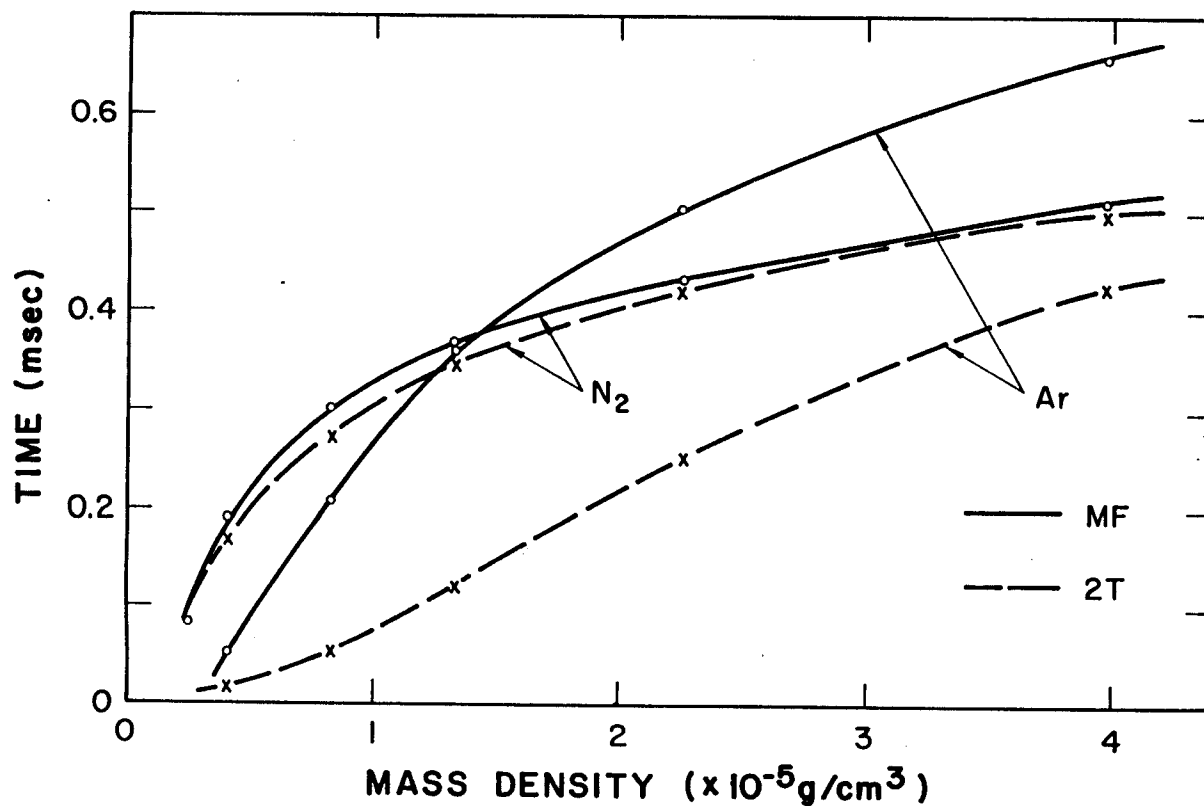Fig. 27. Maximum overpressure at a 3 meter radius first wall for a 200 MJ target explosion.

Fig. 28. Time of maximum overpressure at a 3 meter radius first wall for a 200 MJ target explosion.

the calculational procedure. The hydrodynamic behavior of the Ar gas is also very different between the two models as shown in Figs. 27 and 28.

The differences between the two models can be summarized in three items:

(1) The two-temperature model cannot predict the first early pulse of radiation for the N_2 gas. This is in agreement with Sweeney's calculations [2].

(2) The two-temperature model predicts much larger energy radiated to the wall after the maximum overpressure for the N_2 gas with a mass density below 4.12×10^{-6} g/cm^3 (5 torr at 0°C) than the multifrequency model.

(3) The radiation hydrodynamic behavior of the Ar gas in the two-temperature model is very different from that in the multifrequency model.

These three major differences are discussed in the following sections.

2. The Early Pulse of Radiation for the N_2 Gas in the Multifrequency Model

The time-integrated radiation spectra at the wall just after the first and second pulses are shown in Figs. 29 and 30, respectively, where the mass density of the N_2 gas is 4.12×10^{-6} g/cm^3 (5 torr at 0°C). It is found that the first pulse is composed mainly of hard x-rays (> 400 eV). The second pulse is composed of soft x-rays (< 10 eV). In order to see the radiation diffusion of these hard x-rays, we show the radiation temperature profiles as a function of radius very early in time in the multifrequency and two-temperature models in Figs. 31 and 32. There are two fronts around 80 cm and 150 cm on the profiles (the latter of which will disappear) and the pulse of radiation reaches the wall at 2.63×10^{-8} s through 1.43×10^{-7} s in the multifrequency model. However, there is only one front around 80 cm on the profiles in the two-temperature model. Since the radiation diffusion is dominated by the opacity of the gas, we investigate profiles of the Rosseland
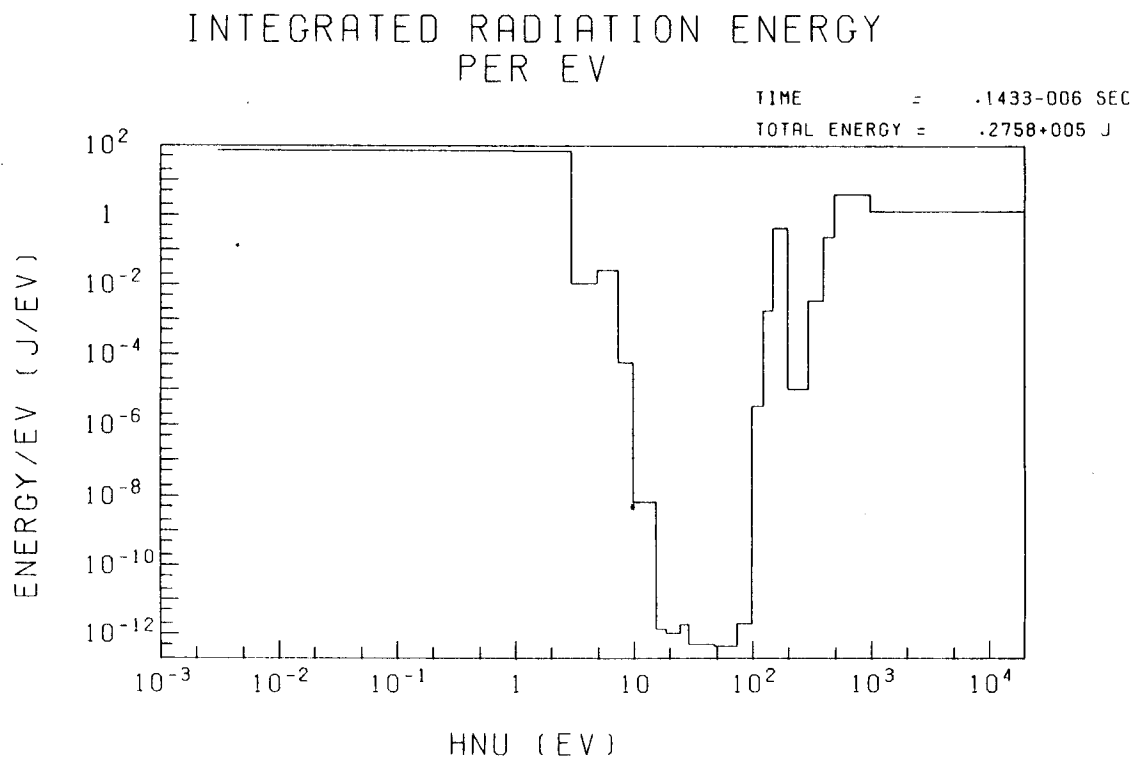
INTEGRATED RADIATION ENERGY
PER EV

TIME   =   .1433-006 SEC
TOTAL ENERGY =   .2758+005 J

Fig. 29. Time-integrated radiation energy spectrum at a 3 meter radius first wall after the first pulse of heat flux for a 200 MJ target yield in 27.3 torr (at 0°C), N_2 gas.

INTEGRATED RADIATION ENERGY
PER EV

TIME   =   .3023-003 SEC
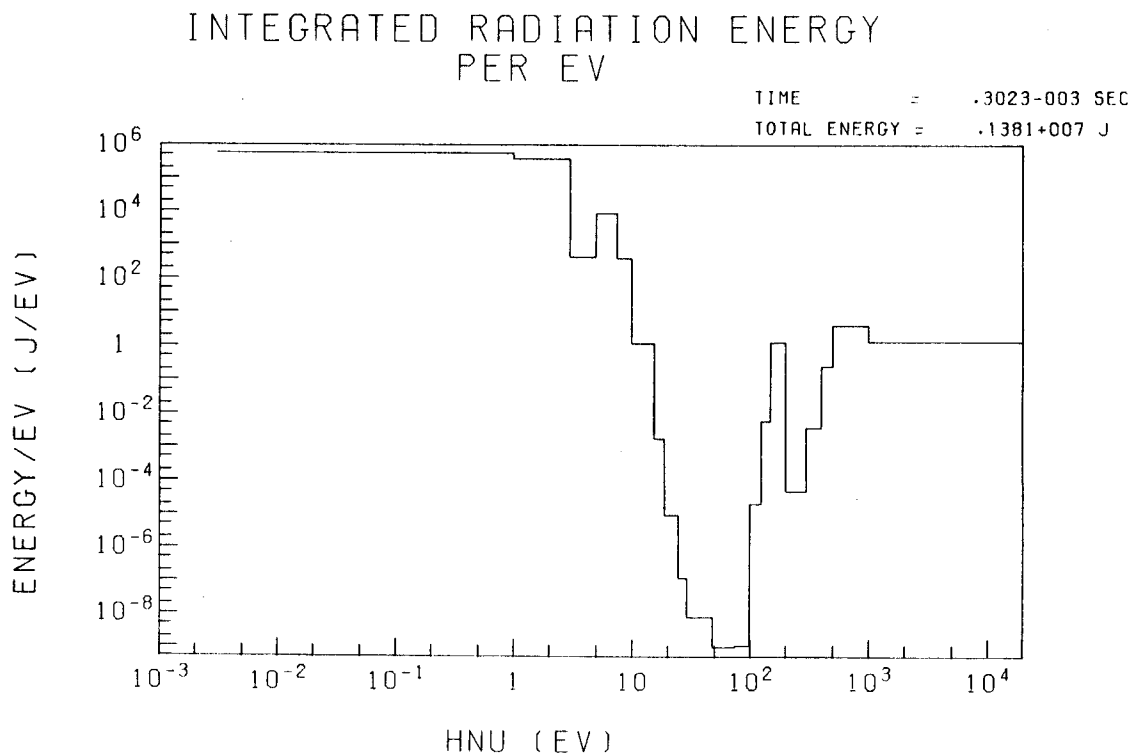TOTAL ENERGY =   .1381+007 J

Fig. 30. Time-integrated radiation energy spectrum at a 3 meter radius first wall after the second pulse of heat flux for a 200 MJ target yield in 27.3 torr (at 0°C), N_2 gas.
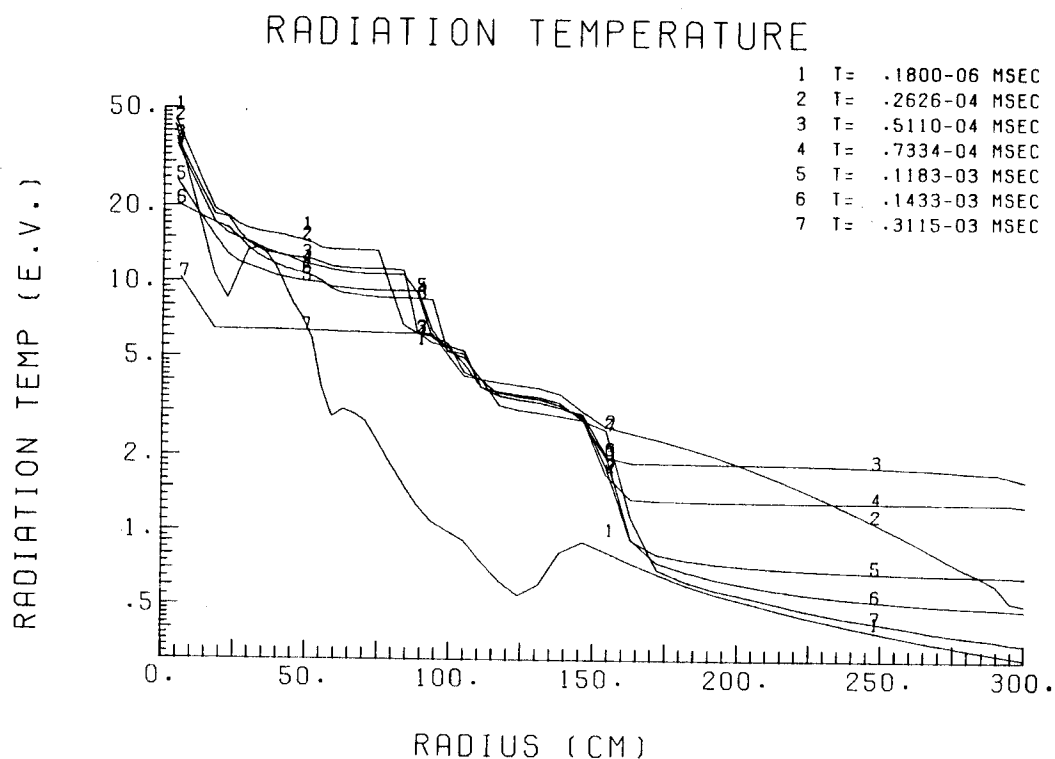
31

RADIATION TEMPERATURE

1	T=	.1800-06	MSEC
2	T=	.2626-04	MSEC
3	T=	.5110-04	MSEC
4	T=	.7334-04	MSEC
5	T=	.1183-03	MSEC
6	T=	.1433-03	MSEC
7	T=	.3115-03	MSEC

Fig. 31. Radiation temperature profiles very early in time in the multi-frequency model for a 200 MJ yield in 27.3 torr (at 0°C), N_2 gas.

RADIATION TEMPERATURE

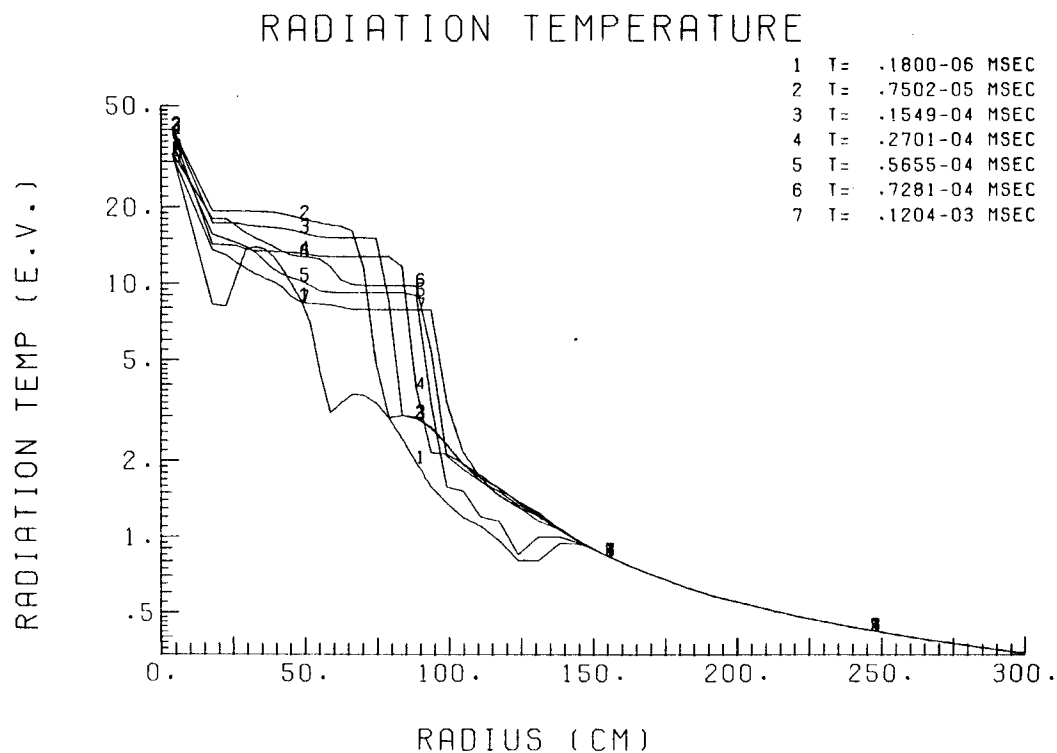|			
1	T=	.1800-06	MSEC
2	T=	.7502-05	MSEC
3	T=	.1549-04	MSEC
4	T=	.2701-04	MSEC
5	T=	.5655-04	MSEC
6	T=	.7281-04	MSEC
7	T=	.1204-03	MSEC

Fig. 32. Radiation temperature profiles very early in time in the two-temperature model for a 200 MJ target yield in 27.3 torr (at 0°C), N_2 gas.

32

opacity and radiation energy spectra at the temperature fronts. The Rosseland opacity is used as a measure of the optical thickness of the gas [16]. Table 4 shows changes of the Rosseland opacities around 80 cm, 150 cm and 200 cm at 2.63×10^{-8} s in the multifrequency model and at 5.66×10^{-8} s in the two-temperature model. A circle (o), a cross (x) and an angle (^) represent sharp increase, sharp decrease and decrease with a small peak as shown below in Table 4. A solid bar in the table indicates the x-ray energy spectrum and a circle on it shows the location of the peak. The details of the radiation energy density spectra at the zones around 80 cm, 150 cm and 200 cm are shown in Figs. 33, 34 and 35. A dotted line represents the blackbody spectrum based on the brightness temperature of each zone. These figures show that the real spectrum is out of equilibrium. The Rosseland opacities of the energy groups between 15.6 eV and 200 eV increase sharply at 80 cm so that the x-rays in these groups are strongly absorbed there as shown in Table 4 and Figs. 33 and 34. However, the x-rays with energies less than 15.6 eV and more than 400 eV can pass through the front since the Rosseland opacity of those energy groups decreases there. The x-rays with energies less than 7.5 eV and more than 400 eV can reach the wall, while the x-rays with energies between 7.5 eV and 15.6 eV are locked up at the second front, 150 cm as shown in Table 4 and Figs. 34 and 35. In the case of the two-temperature model, the frequency-averaged Rosseland opacity increases sharply at 80 cm so that the entire x-ray spectrum is assumed to be absorbed there. This analysis shows that the gas ahead of the fireball is transparent to significant portions of the x-ray spectrum and thus the two-temperature model does not correctly predict the energy diffusion to the first wall.

Table 4. Profile of Rosseland Opacity and Radiation Energy Spectrum
for 200 MJ, 5 Torr, N_2

	Group	Energy Range (ev)	180 cm	150 cm	200 cm
Multigroup	G1	$3 \times 10^{-3} \sim 1$	^	x	x
	2	$1 \sim 3$	^	o	x o
	3	$3 \sim 5$	^	o	x
	4	$5 \sim 7.5$	^	x	x
2.63×10^{-8} sec	5	$7.5 \sim 10$	^	x o	x
	6	$10 \sim 15.6$	^	o	o
	7	$15.6 \sim 19$	o	o	x
	8	$19 \sim 25$	o	x	x
	9	$25 \sim 29.47$	o	x	x
	10	$29.47 \sim 48.7$	o o	x	x
	11	$48.7 \sim 75$	o	x	x
	12	$75 \sim 100$	o	x	x
	13	$100 \sim 125$	o	x	x
	14	$125 \sim 150$	o	x	x
	15	$150 \sim 200$	o	x	x
	16	$200 \sim 300$	x	x	x
	17	$300 \sim 400$	x	x	x
	18	$400 \sim 500$	x	x	x
	19	$500 \sim 1000$	x	x	x
	20	$1000 \sim 20000$	x o	x o	x o
Two-temperature 5.66×10^{-8} sec			o	o	x

o →   x →   ^ →

RADIATION ENERGY DENSITY IN ZONE
PER EV

ZONE = 19
R = 79.4128 CM
TIME = 2.63-005 MSEC

ERREAL = .1118+000 J/CM3
ERBLAC = .1117+000 J/CM3
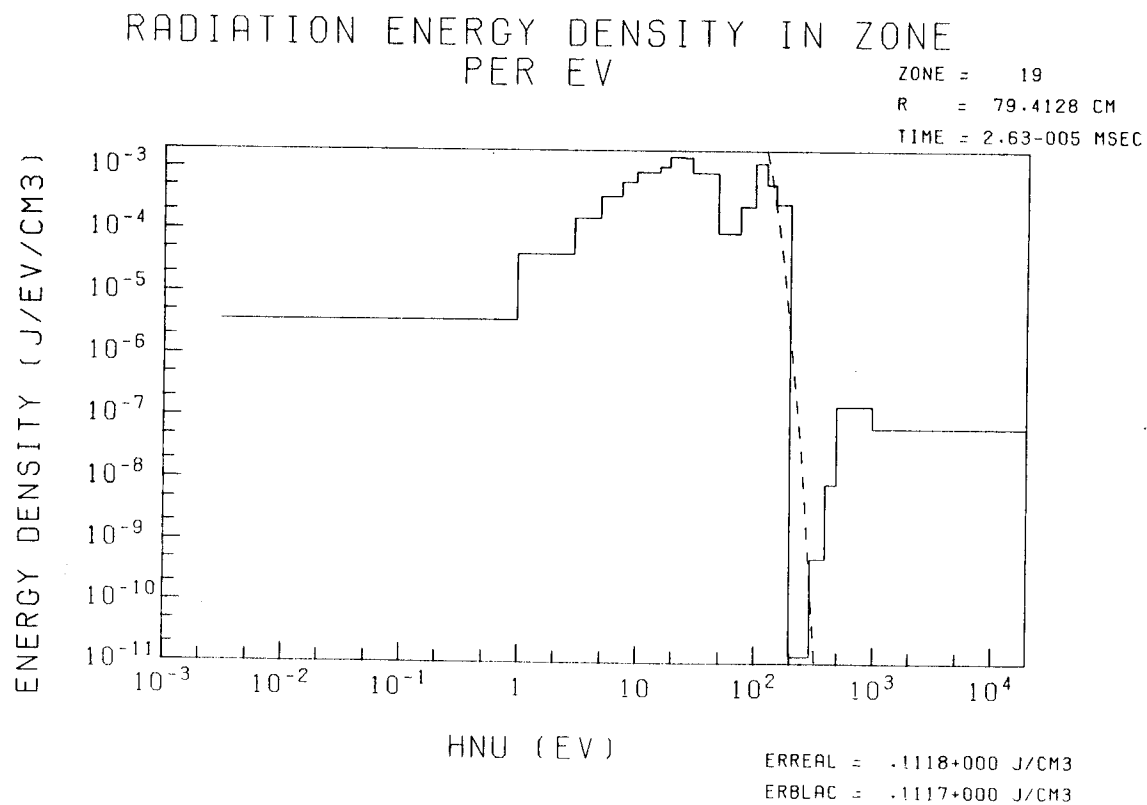
Fig. 33. Radiation energy density spectrum at the radius, R = 79.4 cm, for a 200 MJ target yield in 27.3 torr (at 0°C), N_2 gas.

RADIATION ENERGY DENSITY IN ZONE
PER EV

ZONE = 36
R = 203.3861 CM
TIME = 2.63-005 MSEC

ERREAL = .1512-003 J/CM3
ERBLAC = .1511-003 J/CM3

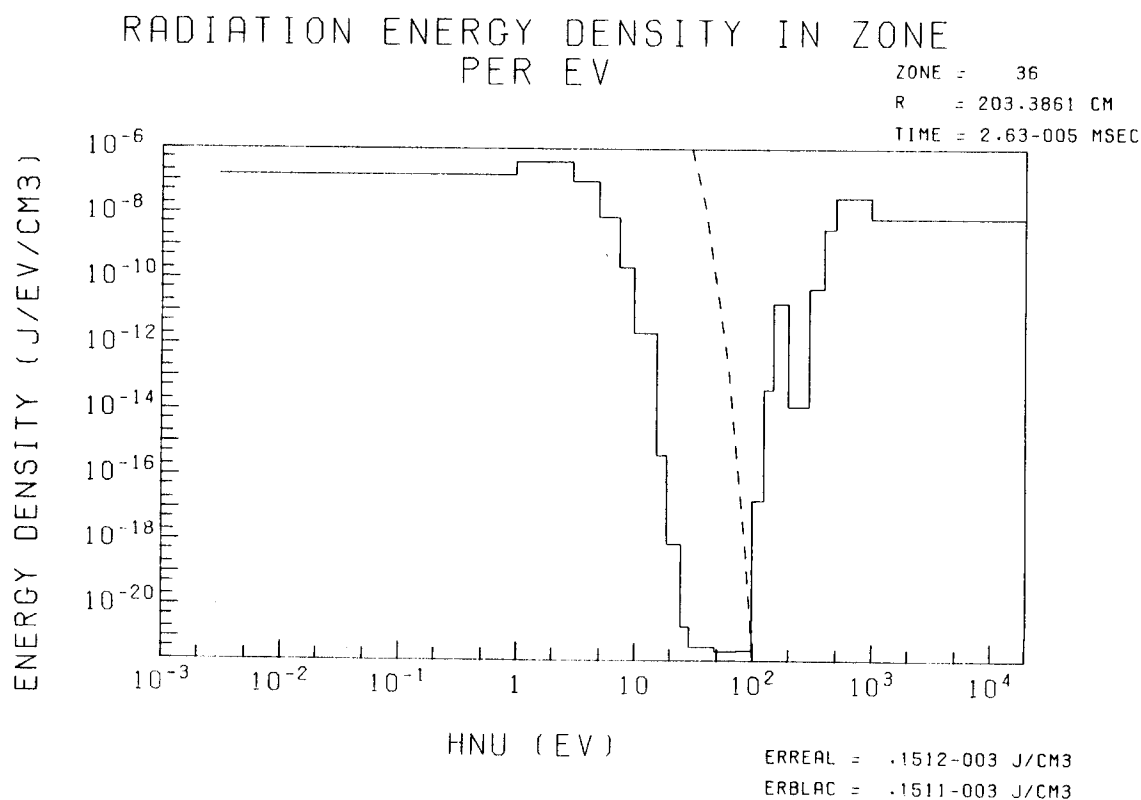Fig. 34. Radiation energy density spectrum at the radius, R = 203 cm, for a 200 MJ target yield in 27.3 torr (at 0°C), N_2 gas.
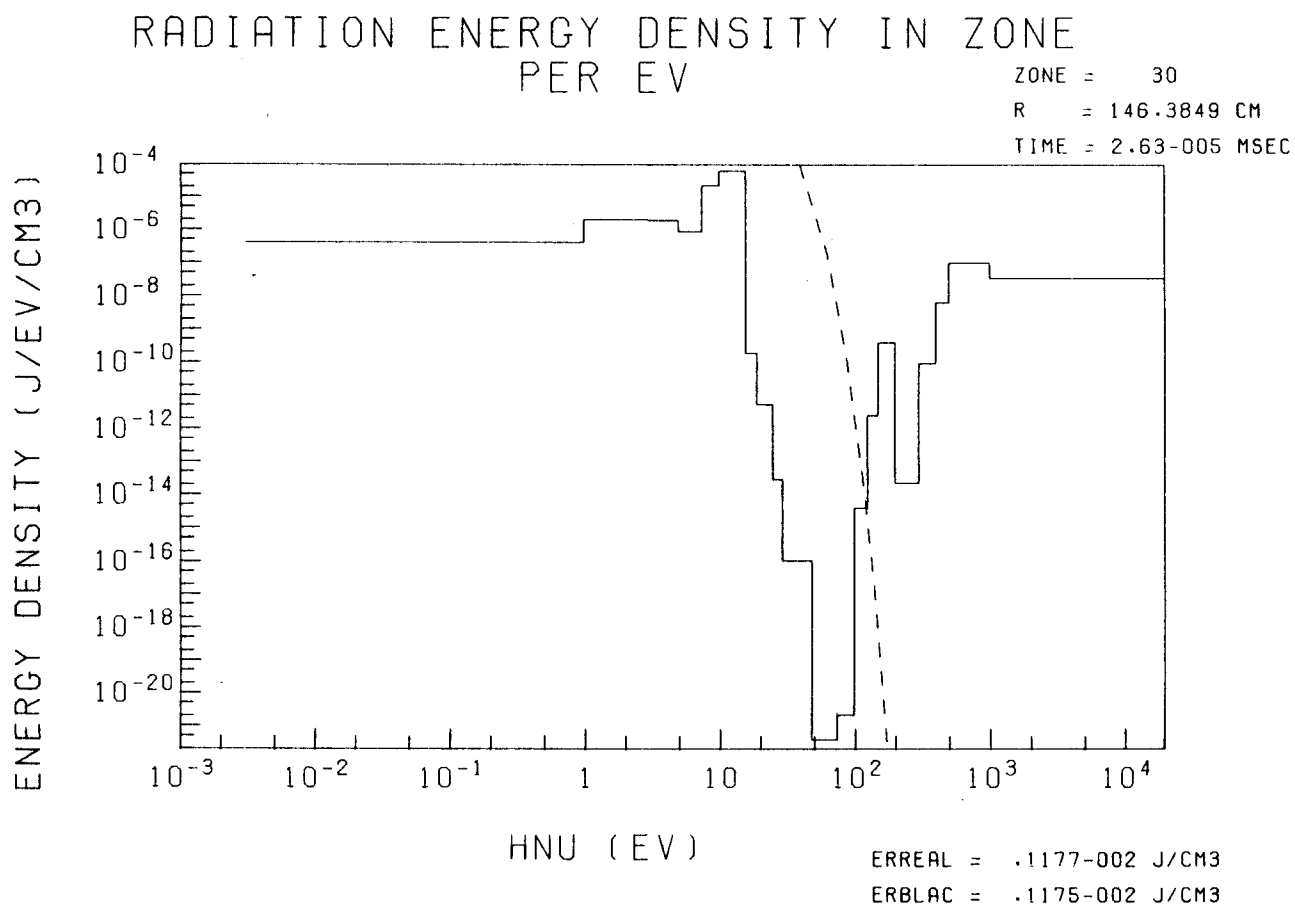
Fig. 35. Radiation energy density spectrum in the zone, R = 146 cm, for a 200 MJ target yield in 27.3 torr (at 0°C), N_2 gas.

3. The Large Energy Radiated to the Wall for the N_2 Gas in the Two-Temperature Model

To determine what factor contributes to the large radiated energy after the maximum overpressure in the two-temperature model, we check the behavior of the energy components of total plasma and radiation energies. Integration of Eqs. (4) and (5) over space and time gives the form,

$$\text{Plasma:} \qquad e_p + T = e_p^0 - E_{PR} \qquad\qquad (11)$$

$$\text{Radiation:} \qquad e_R = E_{PR} - F_R \qquad\qquad (12)$$

where e_p and e_p^0 are the total and initial internal energies of the plasma, e_R is the total internal energy of the radiation, T is the total kinetic energy of the plasma, E_{PR} is the total radiation energy exchanged from the plasma to the radiation, in other words, the difference between the emission and absorption terms, and F_R is the total energy radiated to the wall. Plots of the total exchanged energy (E_{PR}), the total radiated energy at the wall (F_R) and the total internal energy of the plasma (e_p) as a function of time are shown in Figs. 36, 37 and 38. Solid and dotted lines represent the multifrequency and two-temperature cases, and arrows in the figures indicate the times of the maximum overpressure. The other components (T, e_R) are much smaller than the above components by a factor of more than ten. We consider two cases of mass density, 4.12×10^{-6} g/cm^3 and 4.17×10^{-5} g/cm^3 (5 torr and 50 torr at 0°C). In the first case the difference between the multifrequency and two-temperature models is large while in the second case the difference is small. These figures show that the two-temperature model predicts sharp increases of the
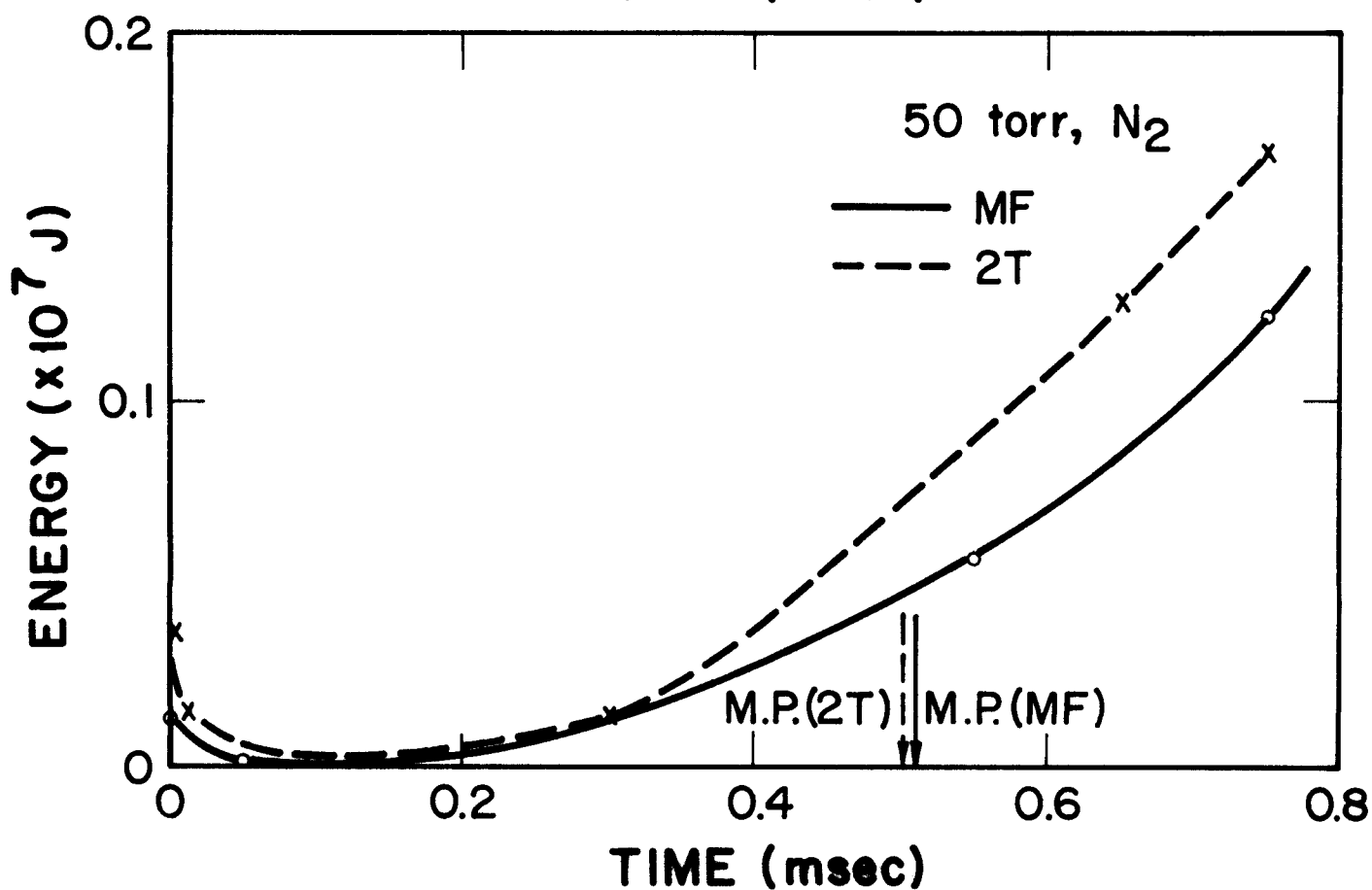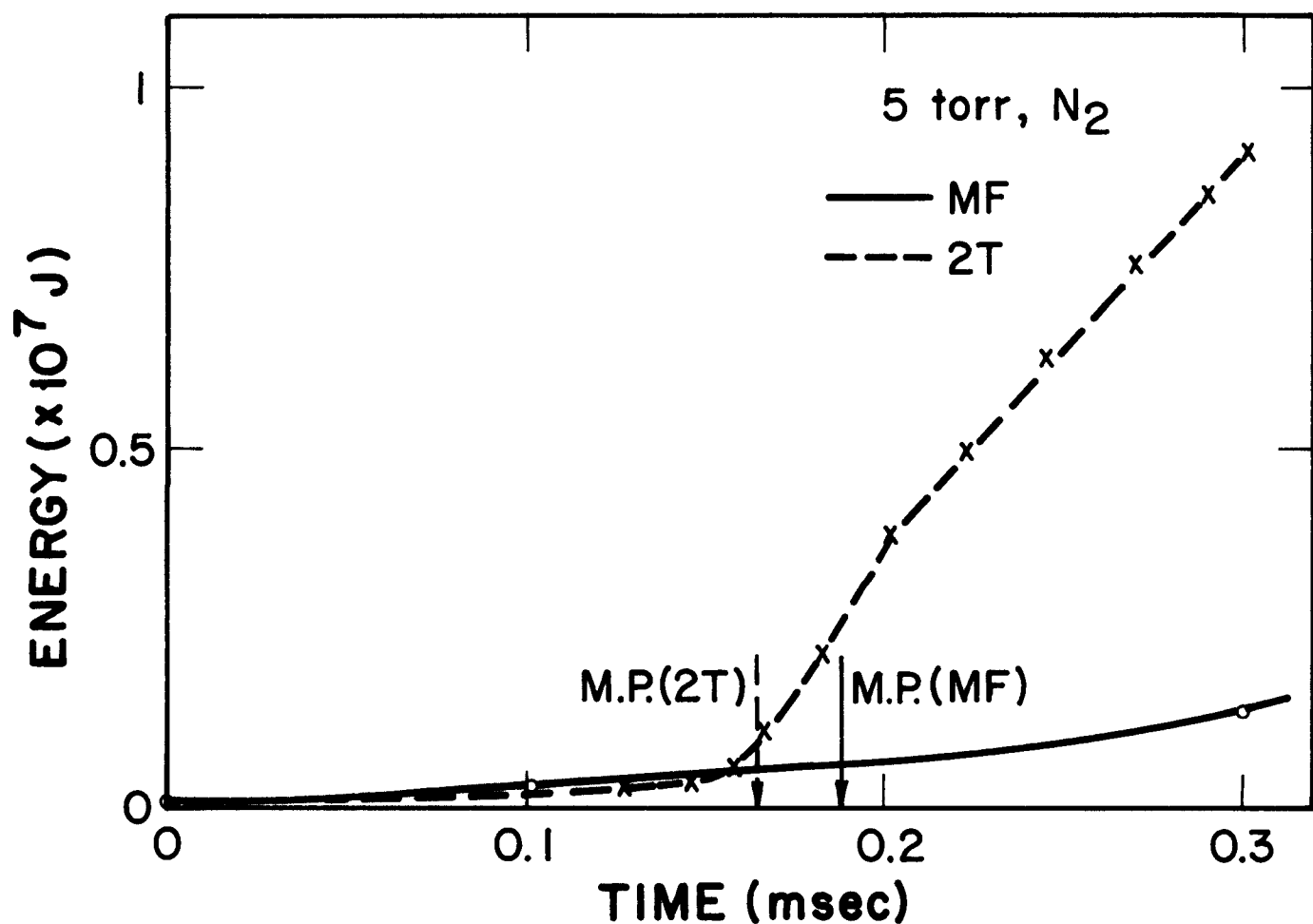
Fig. 36. Energy exchanged from plasma to radiation field vs. time predicted by two-temperature and multifrequency models for a 200 MJ target yield and 5 torr and 50 torr of N_2 gas.
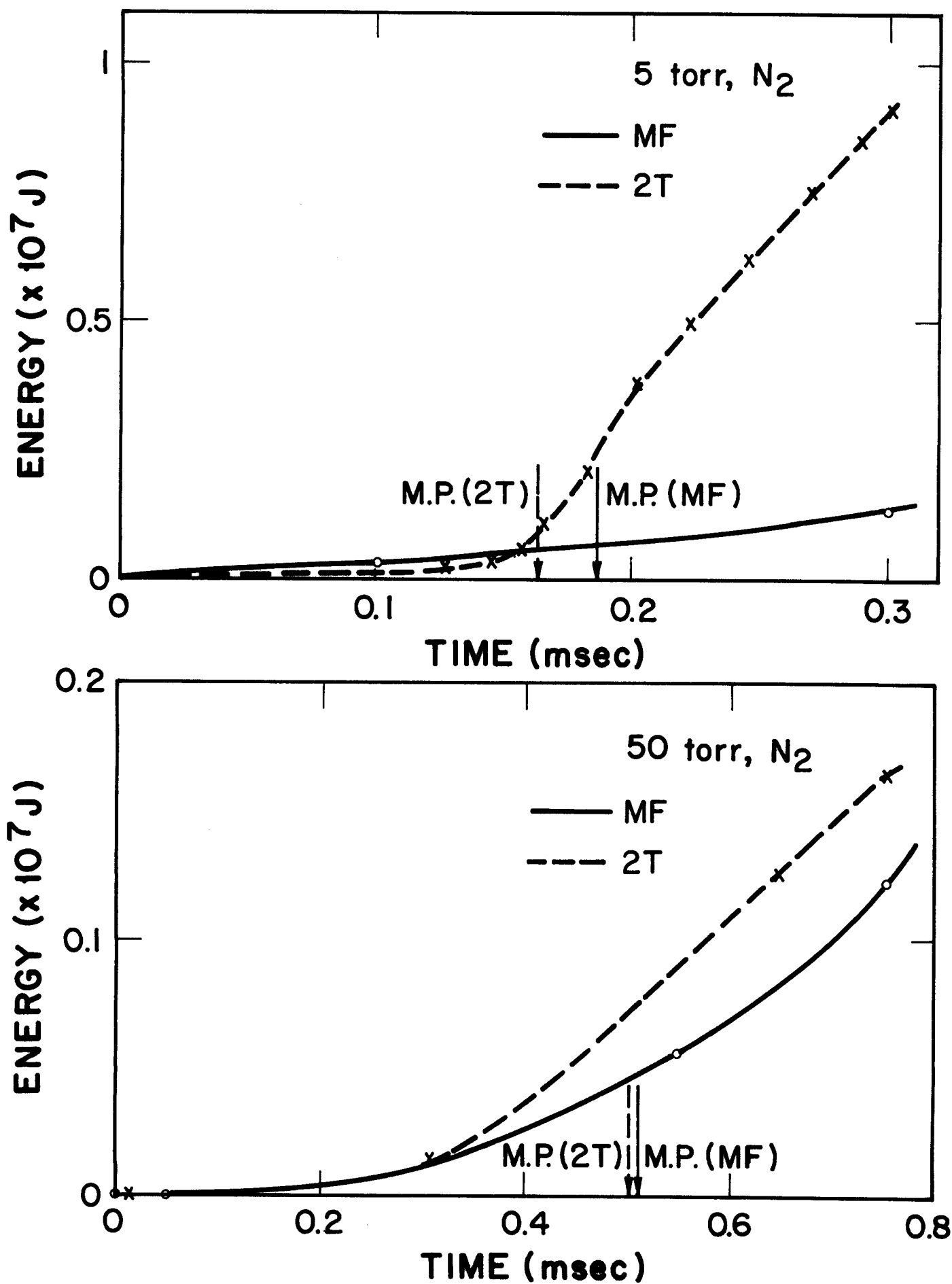
Fig. 37. Radiated energy at the first wall vs. time predicted by the two-temperature and multifrequency models for a 200 MJ target yield and 5 torr and 50 torr of N_2 gas.
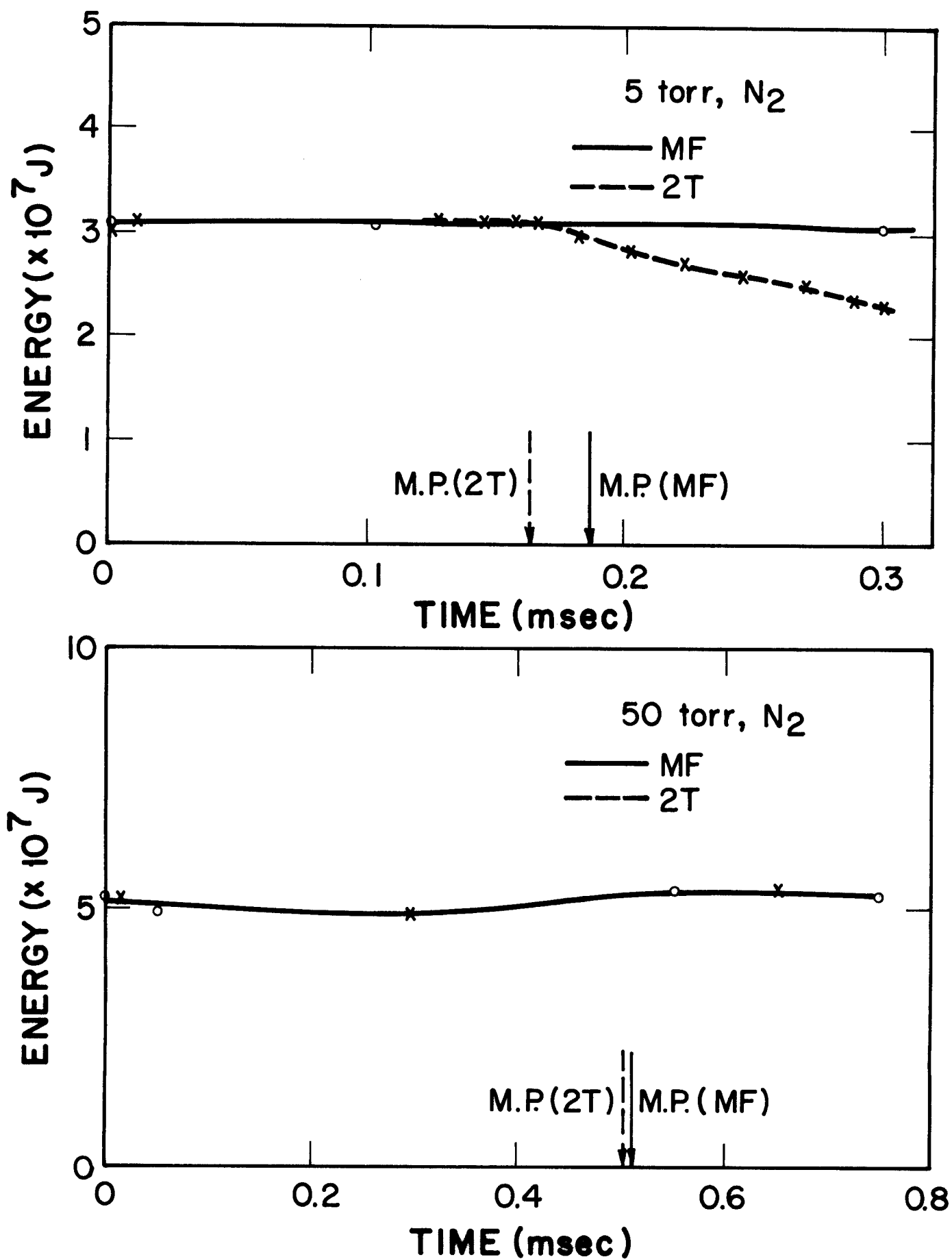
Fig. 38. Plasma internal energy vs. time predicted by the two-temperature and multifrequency models for a 200 MJ target yield and 5 torr and 50 torr of N_2 gas.

exchanged energy and the radiated energy to the wall and sharp decrease of the internal energy of the gas after the maximum overpressure for the case of 4.12 x 10^{-6} g/cm^3. This means the gas emits a large amount of energy as x-rays after the maximum overpressure and these x-rays reach the wall with little absorption. Figure 39 shows plots of the Planck and Rosseland opacities in the zone at R ~ 110 cm, inside the fireball as a function of time around the maximum overpressure for the multifrequency and two-temperature models. The Planck opacity is used as a measure of intensity of emission of the plasma [17]. We use average values for the multifrequency case, using the computed radiation energy spectrum as a weighting function. Figure 40 gives plots of the plasma and radiation temperatures as a function of time in the same zone for the two models. The Rosseland opacity is always underestimated and the Planck opacity increases sharply after the maximum overpressure in the two-temperature model as shown in Fig. 39. The plasma and radiation temperatures in the two-temperature model are smaller than those in the multifrequency model as shown in Fig. 40. Since the Rosseland opacity, i.e. the optical thickness of the plasma is underestimated in the two-temperature model, the plasma cools faster than in the multifrequency model and its temperature reaches ~ 1 eV, where the Planck opacity, i.e. the emission of the plasma, increases sharply. This underestimation of the Rosseland opacity in the two-temperature model is attributable to the deviation of the radiation energy spectrum from the blackbody spectrum, as described in Section III.2, and to the complicated structure of the Rosseland opacity data for radiation energy of a few electrovolts. The large radiated energy to the wall due to the large Planck opacity below the temperature of ~ 1 eV is also observed in the case of 2.50 x 10^{-6} g/cm^3 in the multifrequency model as shown in Fig. 26.
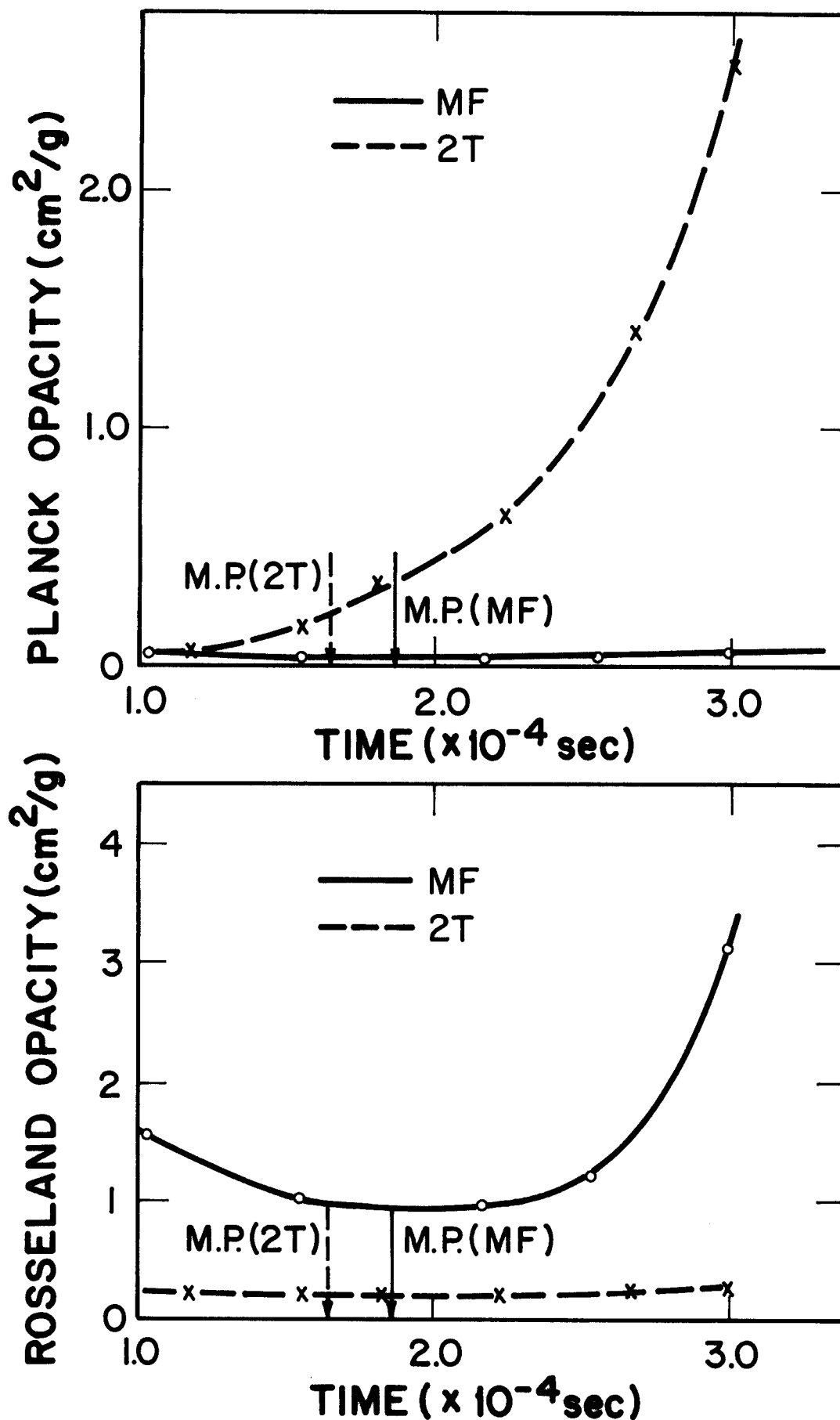
Fig. 39. Planck and Rosseland opacities at R = 110 cm vs. time predicted by the two-temperature and multifrequency models for a 200 MJ target yield and 5 torr and 50 torr of N_2 gas.
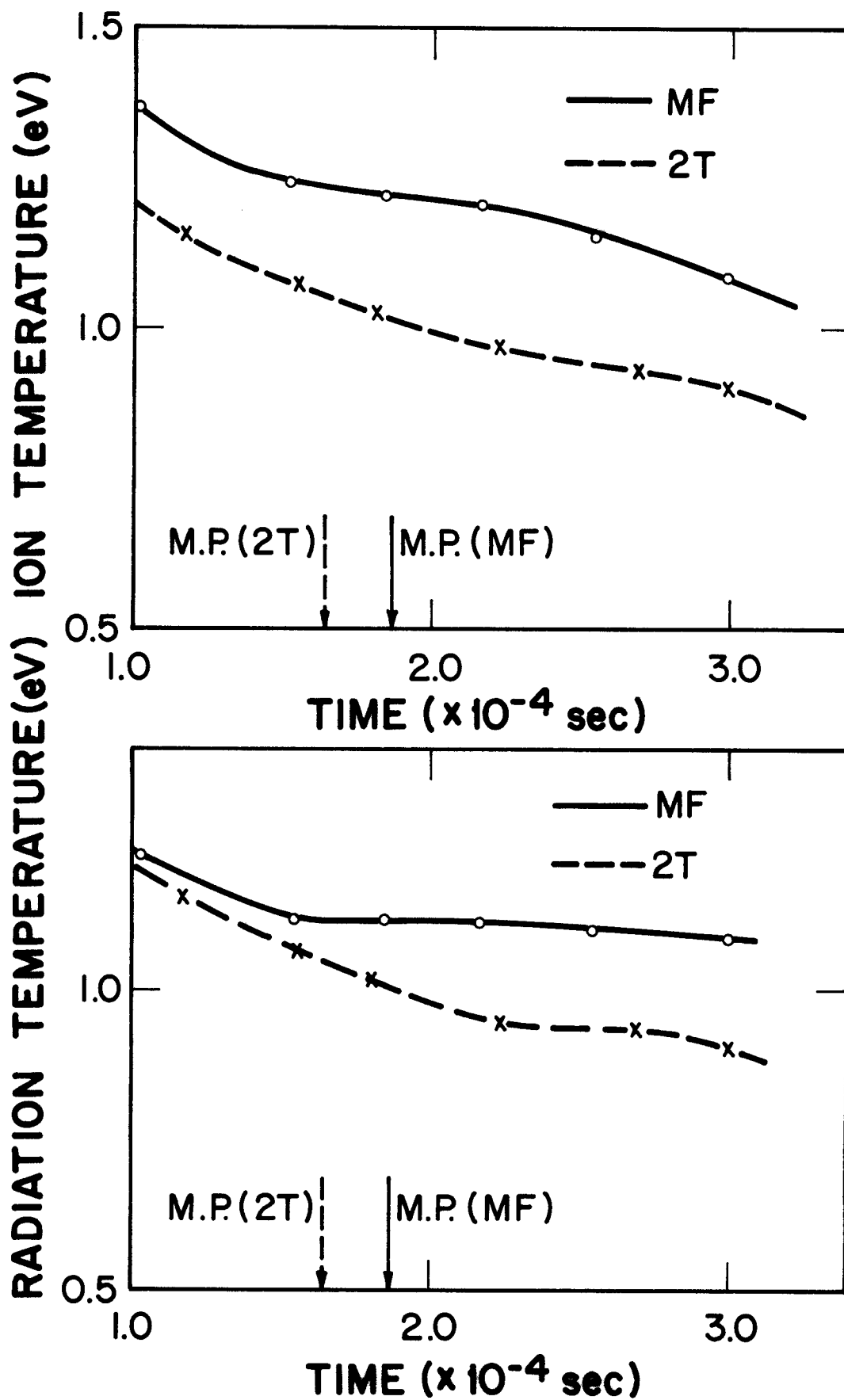
42

Fig. 40. Plasma and radiation temperature at R = 110 cm vs. time predicted by the two-temperature and multifrequency models for a 200 MJ target yield and 5 torr and 50 torr of N_2 gas.

4. The Radiation Hydrodynamic Behavior of the Ar Gas

The hydrodynamic behavior of argon gas is very different for the two models. This is due to the different predictions of the radiation transport. The multifrequency model predicts only one early pulse of radiation, while the two-temperature model predicts one pulse of radiation which reaches the wall together with the pressure wave as described in Section III.1. This difference can be explained by investigating the radiation energy spectrum and the Rosseland opacity in the same way as done in Section III.2. Now, we consider the case of a mass density of 4.12×10^{-6} g/cm^3 (1.85 torr at 0°C). The time-integrated radiation spectra at the wall just after the early pulse and following the reflection of the shock wave from the wall are shown in Figs. 41 and 42. When we compare Fig. 41 with Fig. 29, we find that a large amount of energy between 1 eV and 25 eV reaches the wall in the early pulse in the Ar gas. This is due to the high transparency of the Ar gas for the x-rays (1 eV < E_R < 100 eV) under the condition of plasma density and plasma temperature of this case. The profiles of the radiation temperature very early in time in the two models are given in Figs. 43 and 44. There is a weak front around 80 cm and the pulse of radiation is observed from 1.22×10^{-8} s in Fig. 43, while only a weak front around 80 cm is observed in Fig. 44. Table 5 shows changes of the Rosseland opacities at 80 cm and 200 cm at 2.53×10^{-8} s in the multifrequency model and at 1.35×10^{-8} s in the two-temperature model. Figures 45 and 46 show the radiation energy density spectra at the zones around 80 cm and 200 cm. It is found that there is no sharp increase on the profiles of the Rosseland opacities of the energy groups less than 25 eV and more than 200 eV in Table 5. Hence, a large amount of x-rays in those energy groups can reach the wall with little absorption, while x-rays

Table 5. Profile of Rosseland Opacity and Radiation Energy Spectrum

for 200 MJ, 1.85 Torr, Ar

	Group	Energy Range (eV)	80 cm	200 cm
Multigroup	G1	3×10^{-3} ~ 1	^	x
	2	1 ~ 3	^	x
	3	3 ~ 5	^	x
	4	5 ~ 7.5	^	x
	5	7.5 ~ 10	^	x
2.53×10^{-8} sec	6	10 ~ 15.6	^	x
	7	15.6 ~ 19	^	x
	8	19 ~ 25	^	x o
	9	25 ~ 29.47	^	o
	10	29.47 ~ 48.7	^	x
	11	48.7 ~ 75	^ o	x
	12	75 ~ 100	o	x
	13	100 ~ 125	o	x
	14	125 ~ 150	o	x
	15	150 ~ 200	o	x
	16	200 ~ 300	^	x
	17	300 ~ 400	^	x
	18	400 ~ 500	^	x o
	19	500 ~ 1000	x	x
	20	1000 ~ 20000	x	x
Two-temperature 1.35×10^{-8} sec			o	x

o →   x →   ^ →

INTEGRATED RADIATION ENERGY
PER EV

TIME   =   .2268-006 SEC
TOTAL ENERGY =   .1257+007 J
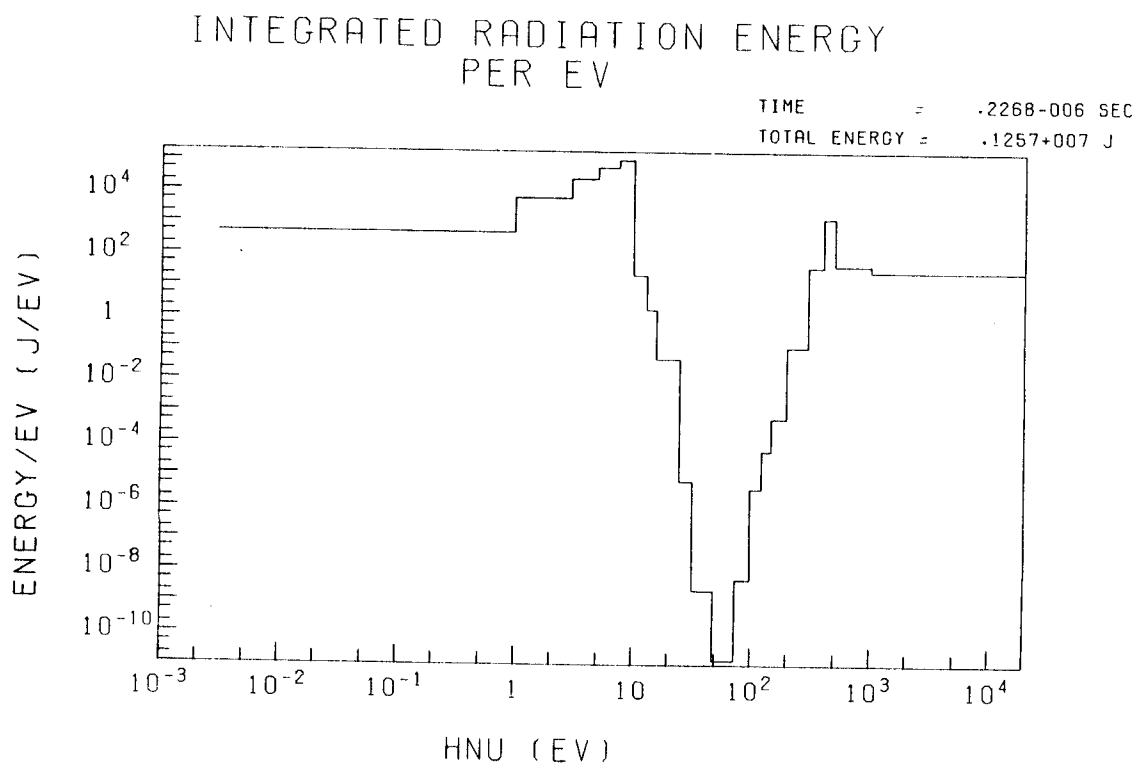
Fig. 41. Time-integrated radiation energy spectrum at a 3 meter radius first wall after the early pulse of heat flux for a 200 MJ target yield in 10.0 torr (at 0°C), Ar gas.

INTEGRATED RADIATION ENERGY
PER EV

TIME   =   .2724-003 SEC
TOTAL ENERGY =   .2804+008 J
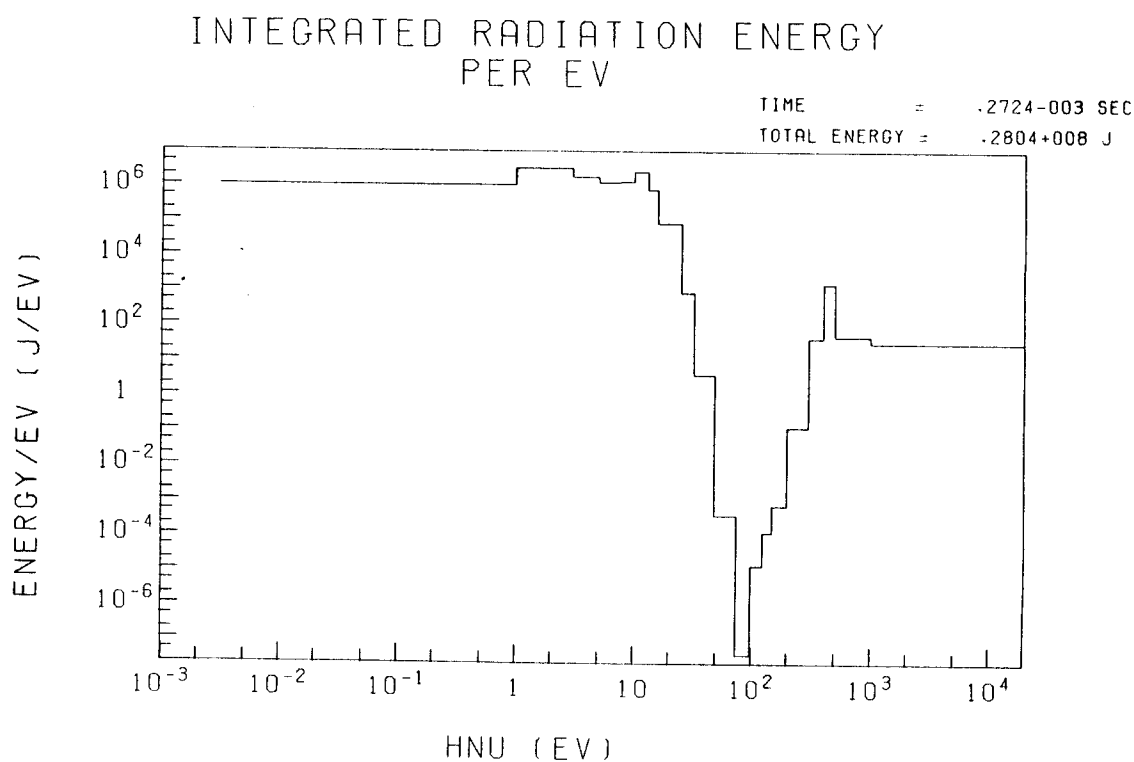
Fig. 42. Time-integrated radiation energy spectrum at a 3 meter radius first wall following the reflection of the shock wave for a 200 MJ target yield in 10.0 torr (at 0°C), Ar gas.

46

RADIATION TEMPERATURE
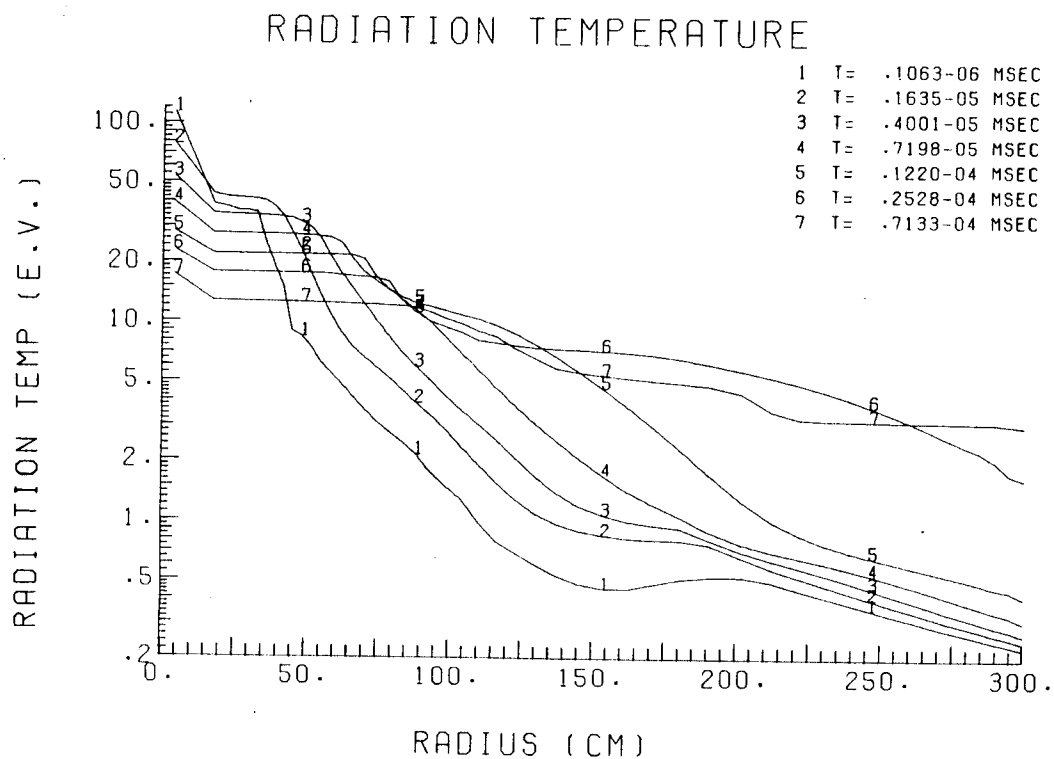
Fig. 43. Radiation temperature profiles very early in time in the multi-frequency model for a 200 MJ target yield in 10.0 torr (at 0°C), Ar gas.

RADIATION TEMPERATURE

Fig. 44. Radiation temperature profiles very early in time in the two-temperature model for a 200 MJ target yield in 10.0 torr (at 0°C), Ar gas.

RADIATION ENERGY DENSITY IN ZONE
PER EV

ZONE = 19
R = 79.0589 CM
TIME = 2.53-005 MSEC

ERREAL = .9024+000 J/CM3
ERBLAC = .9016+000 J/CM3
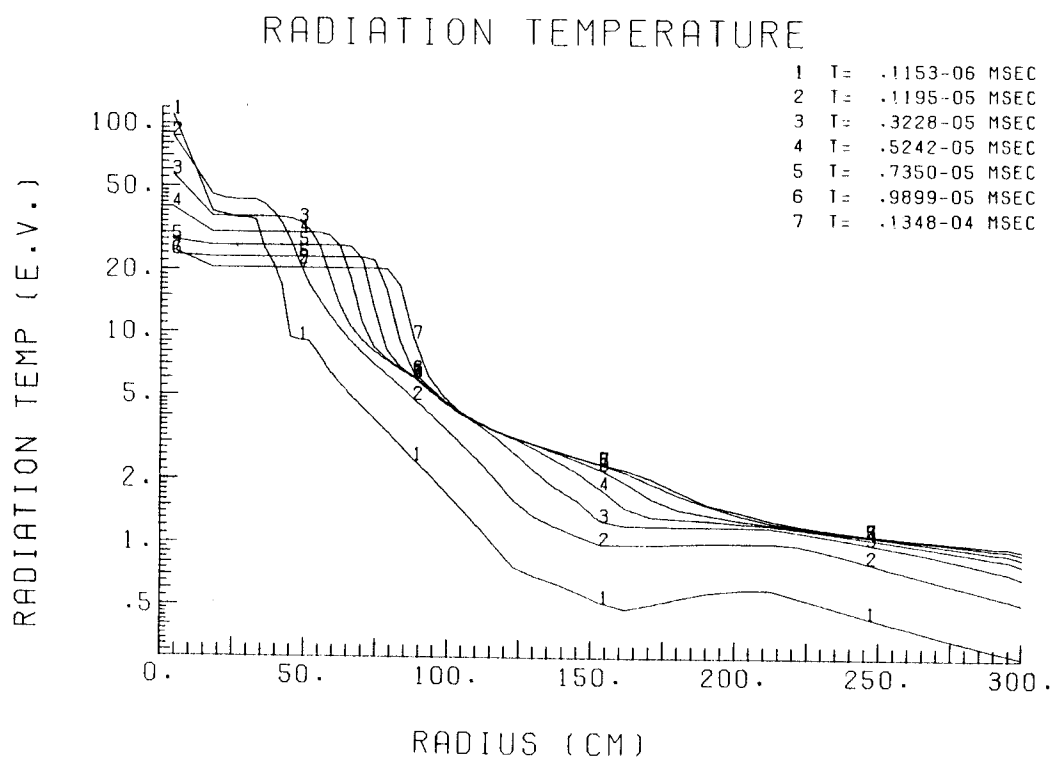
Fig. 45. Radiation energy density spectrum at the radius, R = 79.0 cm, for a
200 MJ target yield in 10.0 torr (at 0°C), Ar gas.

RADIATION ENERGY DENSITY IN ZONE
PER EV

ZONE = 36
R = 201.9029 CM
TIME = 2.53-005 MSEC

ERREAL = .1492-001 J/CM3
ERBLAC = .1491-001 J/CM3
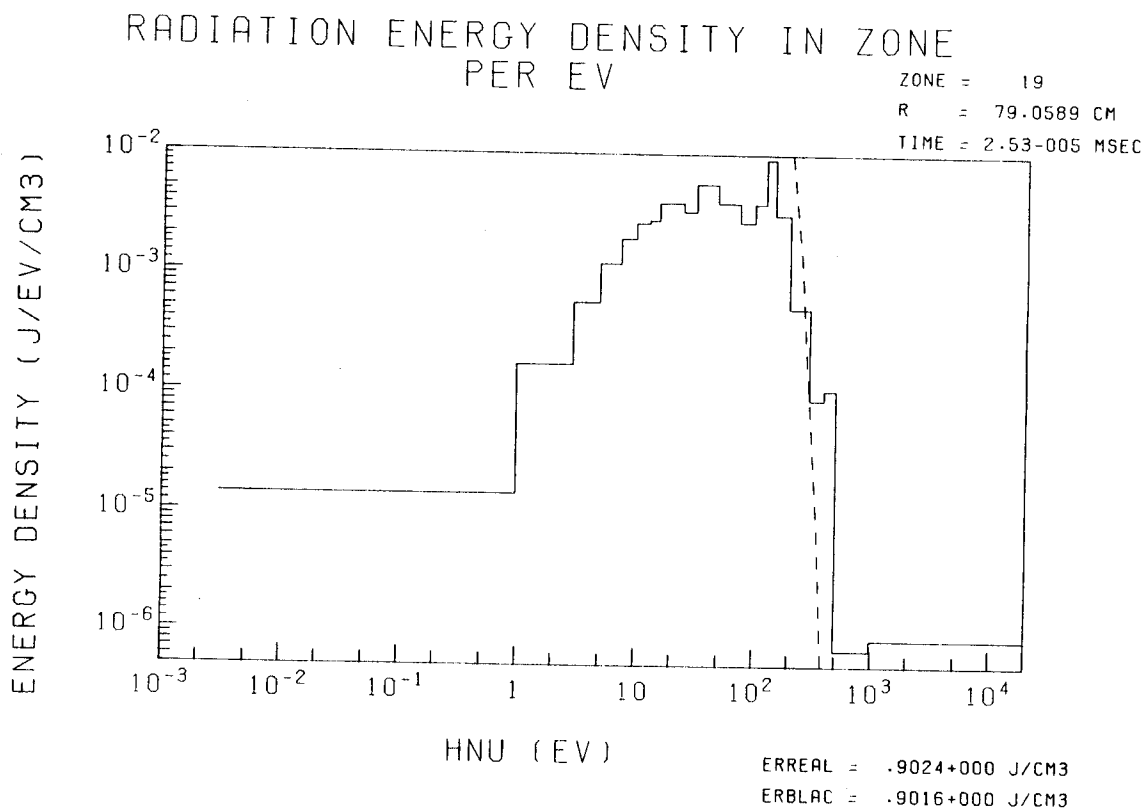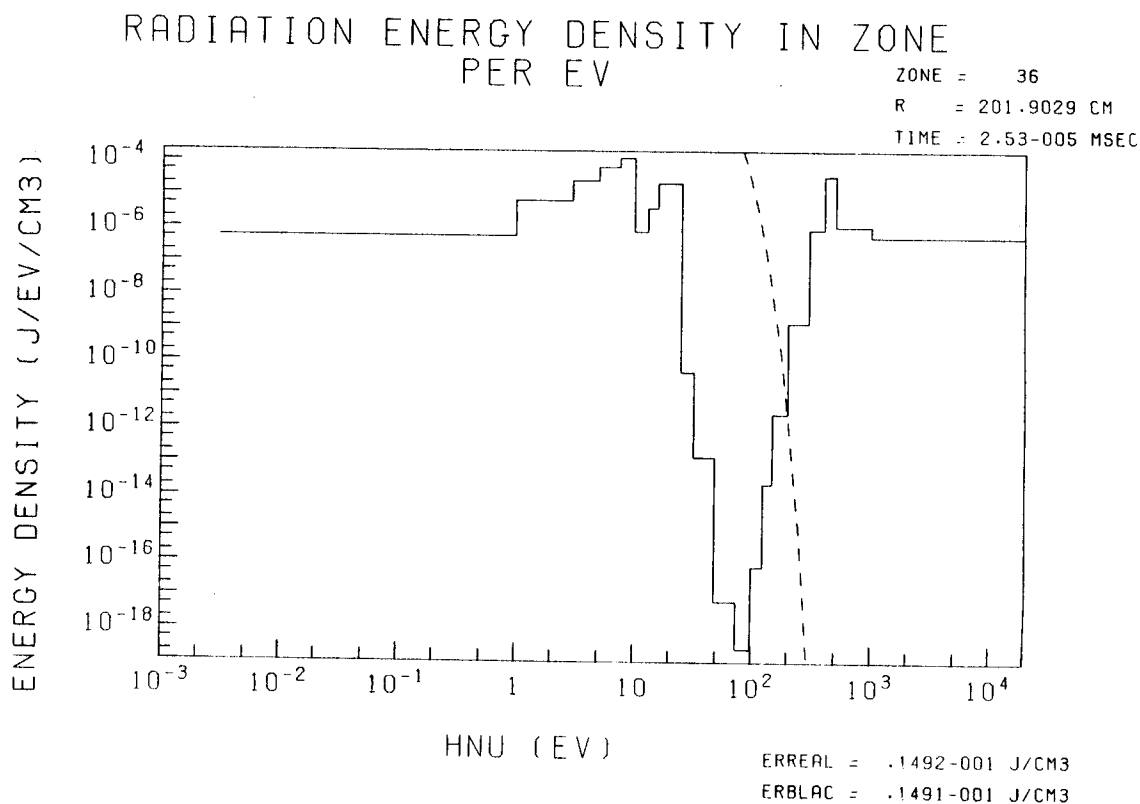
Fig. 46. Radiation energy density spectrum at the radius, R = 202 cm, for a
200 MJ target yield in 10 torr (at 0°C), Ar gas.

(25 eV $< E_R <$ 200 eV) are strongly absorbed at 80 cm as shown in Table 5 and Figs. 45 and 46. However, the frequency-averaged Rosseland opacity in the two-temperature model increases sharply at 80 cm so that the whole x-ray spectrum is absorbed there.

This early release of energy in the multifrequency calculation extends the time of arrival of the shock at the first wall but paradoxically does not weaken the shock pressure. It is interesting that the multifrequency and two-temperature calculations predict roughly the same time-integrated energy release to the wall but the time history of the heat fluxes in each case are considerably different, as discussed above.

IV. Summary and Conclusions

The radiation-hydrodynamics simulation of microfireballs in light ion driven fusion reactors and test facilities has been performed using both a two-temperature and multifrequency approximation to radiative transfer. These calculations were all performed using the MF-FIRE code. In the MF-FIRE code, the one-fluid hydrodynamic approximation is used for the plasma and the one-dimensional equation of motion is expressed in Lagrangian coordinates. The plasma electrons and ions are assumed to be in equilibrium with each other in the plasma temperature equation. In the two-temperature approximation, the radiation is modeled as a fluid with its own local temperature, corresponding to a blackbody frequency spectrum. In the multifrequency approximation the radiation is broken into 20 energy groups and the radiation diffusion equation is solved for each group. The opacity data are provided by the MIXERG code. The initial pellet x-ray energy spectrum obtained from the PHD-IV code is used as an input in the calculation. Then, the thermodynamic state of the gas

after the deposition is used as an initial condition in computing the behavior of the microfireball.

A target yield of 200 MJ is considered for a target chamber 3 m in radius. Both N_2 gas and Ar gas at mass densities ranging from 2.50×10^{-6} g/cm^3 to 4.17×10^{-5} g/cm^3 are considered in this comparison. From these calculations we make the following observations.

(1) For the N_2 gas, the two-temperature approximation fails to predict an early high intense pulse of radiation which is composed mainly of hard x-rays (< 400 eV). This result is in concordance with the earlier results of Sweeney [2]. Although this early pulse of radiation reaches very high intensities (> 1000 kW/cm^2), it contains little energy due to its short pulse width. Hence, it will be important to the accurate calculation of the thermal response of the first wall but does not significantly affect the hydrodynamic behavior of the gas.

2) For the N_2 gas, the two-temperature approximation overpredicts the amount of energy radiated to the first wall following the shock overpressure for gas densities below 4.12×10^{-6} g/cm^3. This was found to be attributable to an underestimation of the Rosseland opacity in the gas near the wall. For gas densities greater than 4.12×10^{-6} g/cm^3 the two-temperature and multigroup calculations give comparable results for total energy radiated to the wall and the magnitude and time of arrival of the shock over-pressure.

3) For the Ar gas, the radiative transfer is significantly different between the two-temperature and multigroup models and this in turn has a large influence on the hydrodynamic behavior of the gas. The multifrequency calculations predict only an early pulse of radiation that contains up to

half of the initial fireball energy while the two-temperature approximation predicts that only about 15% of the fireball energy is radiated to the first wall before the shock wave arrives. This significant loss of fireball energy in the multifrequency prediction does not reduce the maximum overpressure at the wall but lengthens the time of arrival of the shock wave by about a factor of two. We do not yet have an explanation for this phenomena and must investigate it further.

4) For the Ar gas, the total amount of radiated energy to the first wall observed following the shock reflection is about the same (within 20%) for both the two-temperature and multifrequency models. Therefore it is interesting to note that these two models predict about the same value of maximum overpressure and total radiated energy although the detailed time dependence of the radiation hydrodynamics is significantly different.

This careful comparison of the two-temperature and multifrequency modeling of radiative transfer suggests that the simpler two-temperature approximation is adequate for survey calculations of maximum overpressure and total radiated energy for most situations. The exception to this was for N_2 gas at densities below 4.12×10^{-6} g/cm^3 where the two-temperature approximation overpredicted the energy radiated to the wall.

The details of the radiative and hydrodynamic behavior of the gas were in most cases completely different for the two models. Maximum instantaneous heat fluxes, time of arrival of the shock overpressure and the time history of the heat flux are examples of quantities that varied significantly between the two models. Hence, calculations where these quantities are important should be done with the more exact multifrequency model.

Acknowledgment

References

1. J.R. Freeman, L. Baker and D.L. Cook, "Plasma Channels for Intense Light Ion Beam Reactors," Nucl. Fusion 22, 383 (1982).

2. M.A. Sweeney and D.L. Cook, Bull. Am. Phys. Soc. 24, 1072 (1979); M.A. Sweeney, "Particle Beam Fusion Progress Report, January - June 1980," Sandia National Laboratory, Albuquerque, NM.

3. G.A. Moses and R.R. Peterson, "First Wall Protection in Particle Beam Fusion Reactors by Inert Cavity Gases," Nucl. Fusion 20, 849 (1980).

4. R.R. Peterson, G.A. Moses and G.W. Cooper, "Cavity Gas Analysis for Light Ion Beam Fusion Reactors," Nucl. Tech./Fusion 1, 377 (1981).

5. R.R. Peterson, K.J. Lee, G.A. Moses, "Low Density Cavity Gas Fireball Dynamics in the Light Ion Beam Target Development Facility," Proc. of 9th Symp. on Engr. Problems of Fusion Research, Oct. 1981, Chicago, IL, p. 668.

6. R.R. Peterson and G.A. Moses, "Target Explosion Generated Fireballs in the Nitrogen Filled Target Chamber of the Light Ion Fusion Target Development Facility," Proc. of the 5th ANS Top. Mtg. on Fusion Technology, Knoxville, TN, April 1983.

7. M. Uesaka and G.A. Moses, "Parametric Analysis of Microfireballs in the Light Ion Fusion Target Development Facility," University of Wisconsin Fusion Engineering Program Report UWFDM-533 (August 1983).

8. G.A. Moses, T.J. McCarville and R.R. Peterson, "Docmumentation for MF-FIRE, A Multifrequency Radiative Transfer Version of FIRE," University of Wisconsin Fusion Engineering Program Report UWFDM-458 (March 1982).

9. J. Von Neumann and R. Richtmyer, J. Appl. Phys. 21, 232 (1950).

10. L. Spitzer, Physics of Fully Ionized Gases, Second Edition, Interscience Publishers, New York (1962), p. 144.

11. R.R. Peterson and G.A. Moses, "MIXERG - An Equation of State and Opacity Computer Code," University of Wisconsin Fusion Engineering Program Report UWFDM-464 (March 1982).

12. T.J. McCarville, G.A. Moses and G.L. Kulcinski, "A Model for Depositing Inertial Confinement Fusion X-Rays and Pellet Debris into a Cavity Gas," University of Wisconsin Fusion Engineering Program Report UWFDM-406 (April 1981).

13. R. Bangerter and D. Meeker, "Light Ion Beam Driven Target Design," Lawrence Livermore Laboratory Report UCRL-78474 (1976).

14. G. Moses, R. Peterson, M. Sawan, and W. Vogelsang, "High Gain Target Spectra and Energy Partitioning for Ion Beam Fusion Reactor Design Studies," Bull. Am. Phys. Soc. 25, 1013 (1980). Also, University of Wisconsin Fusion Engineering Program Report UWFDM-396, Nov. 1980.

15. G.A. Moses and G.R. Magelssen, "PHD-IV, A Plasma Hydrodynamics-Thermonuclear Burn-Radiative Transfer Computer Code," University of Wisconsin Fusion Engineering Program Report UWFDM-194 (Feb. 1979).

16. V. Zeldovich and Y. Raizer, Physics of Shock Waves and High Temperature Hydrodynamic Phenomena, Academic Press, New York (1966), Vol. 1, p. 154.

17. Ref. (14), Vol. 1, p. 164.